Structural insights into the regulation of acetylation-dependent genome condensation

Ziad Ibrahim[1], Tao Wang[2], Olivier Destaing[2], Nicola Salvi[3], Naghmeh Hoghoughi[2], Alexandra Rusu[1], Jinjun Gao[4], Leonardo Feletto[1], Nicolas Reynoird[2], Thomas Schalch[1], Yingming Zhao[4], Martin Blackledge[3], Saadi Khochbin[2] & Daniel Panne[1,*]

[1]Leicester Institute of Structural and Chemical Biology, Department of Molecular and Cell Biology, University of Leicester, Leicester, UK

[2]CNRS UMR 5309, INSERM U1209, Université Grenoble Alpes, Institute for Advanced Biosciences, Grenoble, France.

[3]Institut de Biologie Structurale, CNRS, CEA, UGA, Grenoble, France

[4]Ben May Department of Cancer Research, The University of Chicago, Chicago, IL 60637, USA.

*Correspondence: daniel.panne@leicester.ac.uk

Summary

Histone modifications are deposited by chromatin modifying enzymes and read out by proteins that recognize the modified state. BRD4-NUT is an oncogenic fusion protein of the acetyl lysine reader BRD4 that binds to the acetylase p300 and enables formation of large hyperacetylated chromatin megadomains. We here examine how reading and writing contribute to larger-scale chromatin architecture. We show that NUT contains an acidic transcriptional activation domain that binds to the TAZ2 domain of p300. We use NMR to investigate the structure of the complex and found that the TAZ2 domain has an autoinhibitory role for p300. NUT-TAZ2 interaction or mutants that interfere with autoinhibition by TAZ2 allosterically activate p300. p300 activation results in a self-organizing, acetylation-dependent feed-forward reaction that enables large-scale intra- and interchromosomal interactions by bromodomain multivalent acetyl-lysine binding. We discuss how the acetylation-dependent read-write reaction drives condensation and the implications for chromatin organisation, gene regulation and dysregulation in disease.

Keywords: Chromatin modification, Acetylation, bromodomain, BRD4, acetyltransferase, p300, transcription factor, activation domain, gene regulation, NMR

Introduction

Chromosome capture experiments have led to the identification of two major mechanisms that are behind large-scale chromosome organisation (Lieberman-Aiden et al., 2009; Schwarzer et al., 2017): (1) at shorter genomic distances, genomes are organized into topologically associating domains (Dixon et al., 2012; Nora et al., 2012) which arise through the process of loop extrusion by cohesin; (2) at longer-range genomic distances, genomes are spatially compartmentalised into active, euchromatic and inactive, heterochromatic regions (Misteli, 2020; Nuebler et al., 2018).

One of the main mechanisms driving genome compartmentalisation is thought to be selective self-association of active or inactive regions and physical constraints including association with architectural elements (Solovei et al., 2016; van de Werken et al., 2017). One hypothesis is that 'readers' of histone modifications seed 'condensation' reactions as a function of the histone modification state (Misteli, 2020; Wang et al., 2019). It has been proposed that compartmentalisation arises specifically due to attractions between heterochromatic regions, possibly driven by polymer-polymer interactions and liquid-liquid phase separation (LLPS) (Erdel and Rippe, 2018; Falk et al., 2019). Whether heterochromatic compartments form through LLPS or other mechanisms is controversial (Erdel et al., 2020; Larson et al., 2017; Strom et al., 2021; Strom et al., 2017).

Histone acetylation counteracts heterochromatinization and has long been associated with chromatin decondensation and euchromatic chromatin regions (Ho et al., 2014). Targeting of heterochromatin with acidic transcription factor (TF) activation domains (ADs) or treatment with deacetylase inhibitors results in hyperacetylation, decondensation and relocation to the nuclear interior even in the absence of active transcription (Carpenter et al., 2005; Chambeyron and Bickmore, 2004; Mueller et al., 2001; Taddei et al., 2001; Therizols et al., 2014; Toth et al., 2004; Tumbar et al., 1999b).

Numerous TFs associate through their ADs with a small set of co-activators including Mediator and the acetylases CBP and its paralogue p300 (also known as KAT3A and KAT3B respectively; hereafter 'p300' for short) (Allen and Taatjes, 2015; Avantaggiati et al., 1996; Green, 2005; Malik and Roeder, 2010; Merika et al., 1998; Reiter et al., 2017). p300 has long been known to be important in integrating multiple signal transduction pathways in the nucleus and enabling enhancer-mediated transcription (Goodman and Smolik, 2000; Kamei et al., 1996; Narita et al., 2021). Intriguingly, it has been proposed that spatial sequestration of heterochromatin at the nuclear lamina requires TF-mediated retention of p300 in euchromatin (Cabianca et al., 2019). Quantitative Mass Spectrometry experiments show that p300 is present at limiting concentrations in the nucleus while HDAC co-repressors are in large excess (Gillespie et al., 2020). As p300 is responsible for up to a third of nuclear acetylation (Weinert et al., 2018), TF-mediated competition for and retention of these essential and limiting co-activators in euchromatic regions could be a key driver event that not only shapes gene specific transcription but also eu- and heterochromatic genome compartmentalisation both locally and globally.

It has been proposed that transcriptional control may be driven by the formation of phase-separated condensates (Hnisz et al., 2017). Accordingly, condensates of TF ADs (Boija et al.,

2018), co-activators and the transcriptional machinery have all been proposed to be relevant for transcriptional regulation (Cho et al., 2018; Chong et al., 2018; Guo et al., 2019; Sabari et al., 2018; Shrinivas et al., 2019; Zamudio et al., 2019). p300 contains an ordered catalytic 'core' domain including a HAT- and bromodomain (BD) and several domains that form promiscuous interactions with the disordered ADs of hundreds of cellular TFs (Fig. 1a) (Delvecchio et al., 2013; Dyson and Wright, 2016). These interactions domains are separated by long, intrinsically disordered regions (IDRs). p300 is activated by autoacetylation (Dancy and Cole, 2015), a reaction that can be controlled by cellular signalling through TF activation and dimerisation (Ortega et al., 2018). The p300 core contains a RING and TAZ2 domain that have an autoinhibitory function (Delvecchio et al., 2013; Ortega et al., 2018). Perturbation of the autoinhibitory function of the RING and TAZ2 domains by mutation leads to constitutive p300 activation and formation of nuclear droplets that co-localise with p53. These droplets are dispersed upon HAT or BD inhibition, suggesting that a form of phase separation (we here use the more general term 'condensation') occurs through an acetylation-dependent 'read-write' mechanism (Ortega et al., 2018). Other data indicate that p300 forms nuclear condensates through the 'core' domain (Zhang et al., 2021). Co-condensation of p300 with TFs on enhancer loci is thought to enable activation of p300's catalytic activity thus allowing the recruitment of acetylation-dependent coactivators, including the BD - and extraterminal domain-containing (BET) protein BRD4 (Ma et al., 2021).

BET proteins have long been associated with the control of large-scale nuclear structure and chromatin organization. BRDT, a testes-specific BET, mediates histone acetylation-dependent chromatin condensation (Pivot-Pajot et al., 2003) and is required for stage-specific gene expression and acetylation-dependent histone removal during spermatogenesis (Gaucher et al., 2012; Goudarzi et al., 2016; Shiota et al., 2018). Similarly, BRD4 has been linked both to gene-specific (Zhao et al., 2011) and higher-order chromatin organisation (Devaiah et al., 2016; Wang et al., 2012b). In yeast, the BET protein BDF1 maintains physical genome barriers by preventing spreading of heterochromatin (Ladurner et al., 2003). *In vitro* data show that under specific buffer conditions, chromatin can undergo LLPS which can be modulated by acetylation and BRD4 binding with BD multivalency being a key determinant factor (Gibson et al., 2019)

BRD4 also forms condensates in cells (Sabari et al., 2018). *In vitro* and *in vivo* experiments with systems inducing high local concentration suggest that a C-terminal IDR drives the condensation reaction (Sabari et al., 2018; Shin et al., 2018). However, a BRD4 isoform lacking the C-terminal IDR also forms condensates in cells (Han et al., 2020). Other data indicate that BRD4 clustering does not depend on IDR-mediated condensation but on DNA and BD-acetyl-lysine recognition which possibly enables long-range enhancer-promoter communication (Li et al., 2020). At a larger scale, such acetylation-dependent long-range interactions could enable selective self-association of euchromatic regions and provide a link between genome topology and gene regulation. It is therefore important to understand the underlying 'read-write' mechanisms that drive such long-range interactions.

BRD4-NUT is an oncogenic fusion protein that drives NUT carcinoma, one of the most aggressive human solid malignancies known (Eagen and French, 2021). NUT is normally expressed in post-meiotic spermatogenic cells, where it interacts with p300 and triggers genome-wide histone hyperacetylation, which enables recruitment of BRDT, histone-to-protamine exchange and chromatin compaction during spermatogenesis (Shiota et al., 2018).

143 In the oncogenic fusion protein, NUT binds to and activates p300 which drives an
144 acetylation- and BRD4 BD-dependent 'feed-forward' loop that leads to formation of
145 hyperacetylated nuclear 'foci' visible by light microscopy (Eagen and French, 2021;
146 Reynoird et al., 2010; Yan et al., 2011), that resemble foci seen in cells expressing
147 constitutively activated p300 (Ortega et al., 2018). These foci correspond to large
148 chromosomal 'megadomains' (100 kb to 2 Mb) that are enriched for BRD4-NUT, p300 and
149 acetylated histones (Alekseyenko et al., 2015; Alekseyenko et al., 2017; Wang and You,
150 2015). Megadomains form in the absence of transcription and engage in very long-range
151 acetylation-dependent inter- and intrachromosomal interactions (Rosencrance et al., 2020).
152
153 The BRD4-NUT model thus exemplifies how a modification of BRD4 enables recruitment
154 and activation of p300 and establishment of a self-organizing feed-forward reaction that
155 results in chromatin hyperacetylation and long-range contact. The underlying mechanisms
156 could have broad implications for our understanding of how 'reading' and 'writing' of
157 chromatin acetylation control gene expression and how dysregulation of this process leads to
158 aggressive forms of disease.
159
160 Here we use the BDR4-NUT/p300 system to dissect the mechanism that drives large-scale
161 chromatin organization. We determined the element of BRD4-NUT required for interaction
162 with p300. We found that the NUT portion of the fusion protein contains an acidic AD that
163 interacts with the p300 TAZ2 domain, a common binding site for numerous TF ADs. We
164 investigate the solution behavior of the complex and found that interaction with the TAZ2
165 domain stimulates p300 HAT activity. Our data indicate that the TAZ2 domain has an auto-
166 inhibitory function that is relieved upon TAZ2 ligand-binding. We systematically probed
167 which elements of BRD4-NUT and p300 drive large scale chromatin condensation in cells.
168 We found that condensation depends on a feed-forward mechanism that involves allosteric
169 activation of p300 by binding of NUT to the p300 TAZ2 domain, nucleation of the
170 condensation reaction through BRD4 and p300 BD-acetyl-lysine binding and that BD
171 multivalency is required. We found that other TAZ2 ligands including p53 and E1A or
172 mutations that interfere with TAZ2 autoinhibition also activate p300. Constitutive activation
173 of p300 is associated with cancer. Our data reveal how activation of p300 establishes a self-
174 organising positive feedback mechanism and how an acetylation-dependent read-write
175 mechanism drives larger-scale chromatin architecture.
176
177 **Results**
178
179 **Identification of an acidic activation domain in NUT**
180 As a first step in characterization of the p300-NUT complex, we examined regions of the two
181 proteins required for interaction (Fig. 1a,b). Previous data showed that a region spanning
182 BRD4-NUT amino acids 347-588 (NUT F1c; NUT numbering is used; 1060-1307 in BRD4-
183 NUT) directly interacts with p300 (Reynoird et al., 2010). To map the interaction further, we
184 produced a series of deletions within NUT and assayed their interaction with p300 using co-
185 sedimentation and GST pulldown assays. NUT fragments that contained amino acids 427-
186 527 generally co-sedimented with the p300 core-CH3, the isolated p300 CH3 or TAZ2
187 domains (Fig. S1a,b; Fig. S2a-e).
188
189 The TAZ2 domain forms dynamic interactions with short ~30 amino acid transcription factor
190 activation domains (ADs) that are unrelated in sequence but generally share net negative
191 charge, hydrophobic, and aromatic residues that are typically intrinsically disordered (IDR) in
192 isolation (Dyson and Wright, 2016). Accordingly, sequence analysis revealed that the region

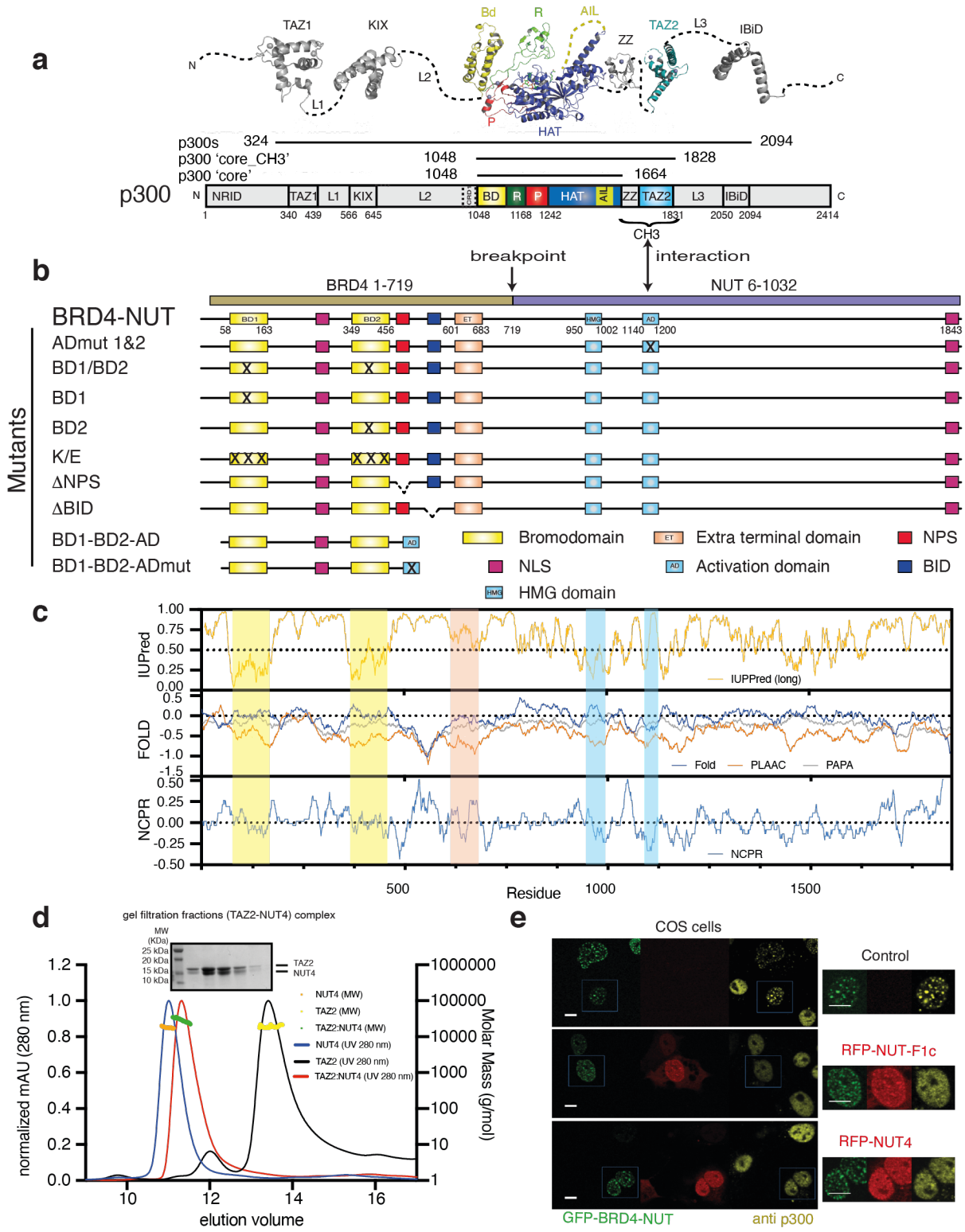

Figure 1. Identification of an acidic activation domain in NUT. **a**, Domain structure of p300 and **b**, BRD4-NUT constructs. **c,** IUPred, prediction of intrinsic disorder; FOLD, folding prediction using the foldindex (blue), PLAAC (**P**rion-**L**ike **A**mino **A**cid **C**omposition; orange) and PAPA (**P**rion **A**ggregation **P**rediction **A**lgorithm; gray) analysis, NCPR (**N**et **C**harge **P**er **R**esidue with a sliding window of 10 residues of the BRD4-NUT protein. **d**, SEC-MALLS analysis of the TAZ2 domain of p300 alone (black), NUT4 alone (blue) and the complex between TAZ2 and NUT4 (red). SDS-PAGE analysis of the peak fractions of the TAZ2-NUT4 complex is shown. **e,** Competition analysis: Cos7 cells were transfected with constructs expressing GFP-BRD4-NUT (green) alone or co-transfected with RFP-NUT-F1c and RFP-NUT4 (red). Immunofluorescence with anti-p300 antibody was used to visualize endogenous p300. Scale bars, 10 μm.

193 of NUT is predicted to be disordered, and negatively charged with modest propensity to self-
194 aggregate (Fig. 1c). A luciferase assay confirmed that the isolated NUT region can stimulate
195 transcription (Fig. S1c), in agreement with previous data showing that tethering of NUT on
196 chromatin is sufficient to induce transcriptional activation (Wang and You, 2015). We
197 therefore conclude that NUT contains an acidic AD that directly interacts with the TAZ2
198 domain of p300 (Fig. 1b).
199
200 The high percentage of negatively charged amino acid residues in ADs is thought to prevent
201 hydrophobic collapse while the distribution of charges maintains the conformational
202 ensemble in a more expanded state leaving the charged and hydrophobic side chains exposed
203 to the solvent and binding partners (Staller et al., 2018). Accordingly, analysis by size-
204 exclusion chromatography–multi-angle laser-light scattering (SEC–MALS) showed that a
205 NUT fragment spanning amino acids 347-480 (NUT4) is monomeric and monodisperse in
206 solution with a large hydrodynamic radius, consistent with an extended conformation (Fig.
207 1d). The TAZ2:NUT4 complex formed a 1:1 complex with a reduced hydrodynamic radius,
208 indicative of conformational compaction upon binding (Fig. 1d).
209
210 Co-expression of NUT F1c can prevent condensate formation in the nucleus by acting as a
211 dominant negative inhibitor for the p300-NUT interaction (Reynoird et al., 2010; Wang and
212 You, 2015). Accordingly, overexpression of RFP-NUT F1c, -NUT4, or -NUT2 but not -
213 NUT1 or -NUT3 reduced p300 foci in COS cells (Fig. 1e, Fig. S2g). As AD function is
214 usually confined to short sequences, we further mapped the interaction by limited proteolysis
215 followed by in-gel acid hydrolysis and mass spectroscopy (Fig. S1d). This led to an
216 additional series of constructs that all bound the TAZ2 domain (Table 1). Fragments
217 spanning amino acids 396-482 (NUT9) or a peptide spanning 458-482 (NUT10) all bound to
218 the TAZ2 domain (Table 1).
219
220 **TAZ2-NUT interaction.**
221 NMR spectra of NUT7, spanning 448-492, feature little dispersion of ^{1}H resonances (Fig.
222 2a), indicating that the protein is largely disordered in solution. We used a series of 3D
223 experiments (see Methods) to assign backbone resonances of NUT7. Secondary structure
224 propensities (SSP) calculated using ^{13}Cα, ^{13}C' and ^{15}N chemical shifts show that amino acids
225 451-472 have a significant tendency to sample helical conformations in solution (Fig. 2b).
226 We conclude that the NUT7 AD is an IDR in isolation with a pre-organised N-terminal α
227 helix.
228
229 We monitored binding to the TAZ2 domain by collecting a series of ^{1}H, ^{15}N-HSQC spectra
230 of ^{15}N-labeled NUT7 mixed with increasing concentrations of TAZ2 (Fig. 2a). Chemical shift
231 perturbations (CSP) showed that several NUT7 backbone amide resonances, including A450,
232 L451, G460-A464, V467 and E475 were perturbed upon addition of an equimolar amount of
233 TAZ2 while resonances from the C-terminus of NUT7 do not appear to shift significantly
234 upon addition of TAZ2 (Fig. 2c). Thus, the N-terminal α-helical segment of NUT7 is
235 involved in TAZ2 binding. Addition of equimolar amounts of unlabelled NUT7 to ^{15}N-
236 labeled TAZ2 showed significant CSPs of resonances corresponding to residues R1737,
237 I1739, M1761, R1763, V1765, Q1766, T1768, K1783, Q1784, I1809 (Fig. 2a, c), that are
238 mostly located on the surface of TAZ2.
239
240 To understand the binding mode, we measured both ^{13}C- and ^{15}N-HSQC-NOESY spectra on
241 a sample of ^{15}N,^{13}C-labelled TAZ2 to which one equivalent of unlabelled NUT7 was added.
242 We also measured ^{15}N-HSQC-NOESY spectra on ^{15}N-labelled NUT7 in admixture with one

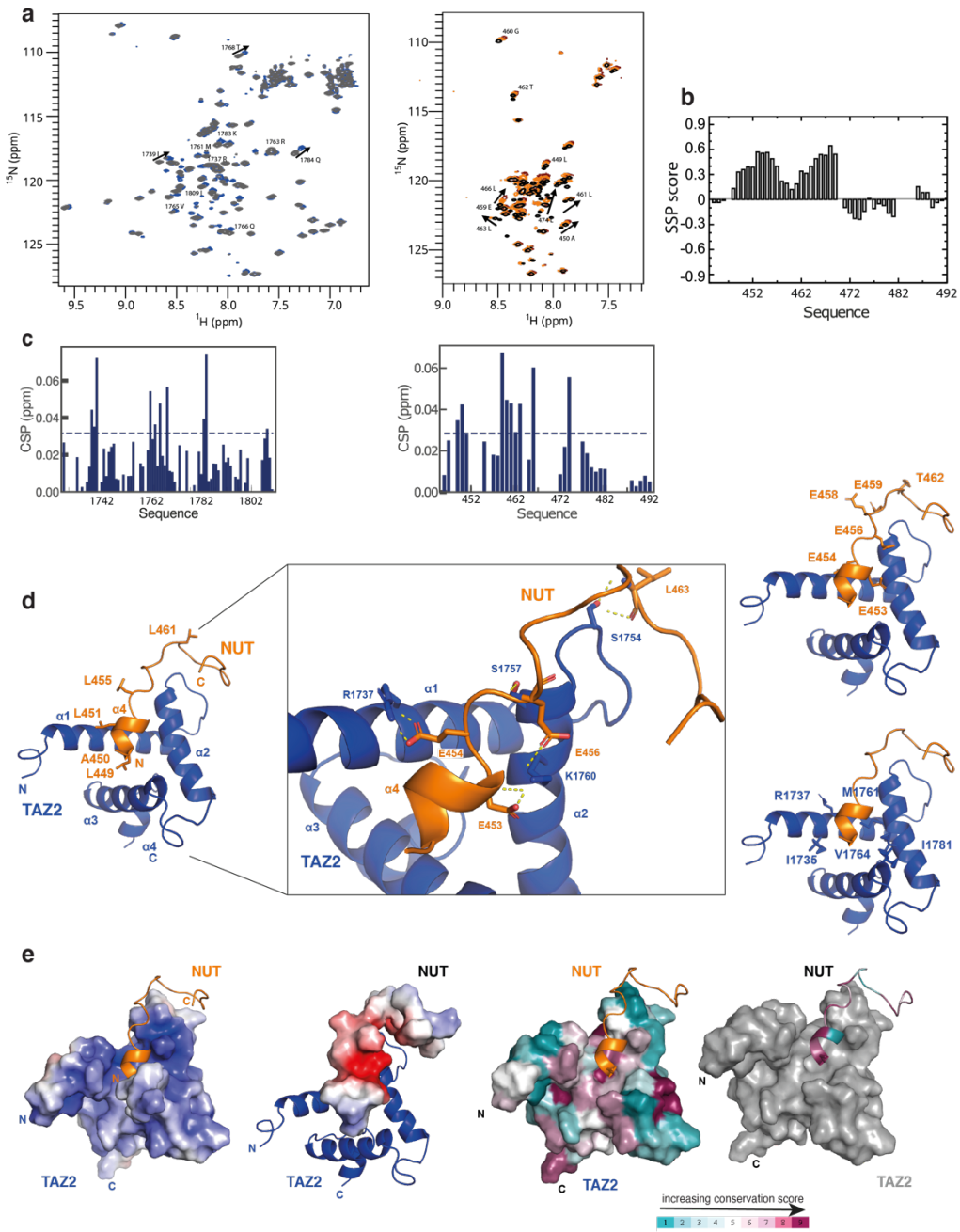

Figure 2. TAZ2:NUT interaction. **a**, (Left) Overlay of ^{1}H-^{15}N HSQC spectra of free TAZ2 (black) and after addition of one molar equivalent of NUT7 (448-492) (blue). Arrows indicate chemical shift changes for individual cross-peaks. (Right) Overlay of ^{1}H-^{15}N HSQC spectra of free NUT7 (448-492) and after adding half (orange) and one (brown) molar equivalent of TAZ2. Arrows indicate chemical shift changes for individual cross-peaks. **b**, Secondary structure propensities (SSP) plot of the NUT (448-492) fragment in its free state. positive values on the Y-axis indicate a-helical propensity, the X-axis is the amino acid sequence. **c**, (Left) Chemical shift perturbations on TAZ2 upon adding one molar equivalent of unlabeled NUT7 (448-492). (Right) Chemical shift perturbations on NUT7 (448-492) upon adding one molar equivalent of unlabeled TAZ2. **d**, (Left) Ribbon representation of lowest energy NMR model of the TAZ2 (blue)-NUT (orange) complex. Hydrophobic residues on the surface of NUT are shown. (middle) Zoom-in view of the interface between NUT (orange) and TAZ2 (blue). Residues on both sides implicated in the interaction as well as the hydrogen bonding network are shown. (Right) acidic residues on the surface of NUT (top) as well as hydrophobic and basic residues on the surface of TAZ2 (bottom) are shown. **e,** TAZ2 and NUT7 (448-492) are surface rendered and colored according to electrostatic potential (left) and sequence conservation (right).

243 equivalent of unlabelled TAZ2. The NOESY spectra contain very few cross-peaks that can be
244 unambiguously assigned to intermolecular contacts most likely due to extensive dynamic
245 fluctuations of NUT7 even in the bound state. One contact is made between the backbone
246 amide hydrogen of S1726 in TAZ2 and the backbone amide hydrogen of residue L463 and
247 the Hβ of A464 in NUT7. Because of relative sparsity and ambiguity of structural restraints,
248 we used HADDOCK (Dominguez et al., 2003) to derive a structural model of the interaction
249 consistent with the observed spectroscopic changes (Fig. 2d and e). NMR restraints and
250 structural statistics are summarized in Table 2. On the basis of this model, it appears that the
251 N-terminus of NUT7 folds into an amphipathic helix that binds a hydrophobic groove in the
252 interface between helices α1/α2/α3 on the surface of TAZ2 (Fig. 2d). Only the NUT
253 backbone residues P448 to A464 are well ordered while residues at the C-terminus (Q465-
254 D492) do not interact with TAZ2 and remain disordered. A set of hydrophobic side chains of
255 NUT L449, A450, L451, L455, L461 are in contact with TAZ2 residues I1735, M1761,
256 V1764, I1781 (Fig. 2d). The interaction appears to be further stabilised by electrostatic
257 interactions involving NUT residues E453, E454, E456, E458, E459 and TAZ2 residues
258 R1737, S1754, S1757 and K1760 (Fig. 2d). In order to test our model, we mutated amino
259 acids that, according to the model, are not interacting with TAZ2 (E459A, L466A and
260 L474A), These mutations have very limited impact on the HSQC spectrum of TAZ2 in
261 complex with NUT7, indicating that the mutant has the same binding mode as the wild-type
262 construct (Fig. S3d). In summary, similar to other TAZ2:AD interactions, a positively
263 charged TAZ2 domain interacts with a negatively charged NUT AD (Fig. 2e). The key
264 interfacial binding surfaces are conserved in p300 and NUT (Fig. 2e).
265
266 **Analysis of the TAZ2:NUT interaction**
267 As ADs are frequently bi-partite and the NUT7 fragment in our structure only partially
268 engages the TAZ2 binding surface, we further explored the region N-terminal of NUT7. We
269 found using HSQC competition, that the NUT7 fragment is unable to displace p53 from the
270 surface of TAZ2 when added to the complex (Fig. S3e). Biolayer Interferometry (BLI)
271 experiments showed that NUT8 (396-470) bound to TAZ2 with a dissociation constant of K_d
272 = 0.96 +/- 0.29 μM (Fig. 3a, b). Alanine substitutions of conserved residues in the region
273 spanning 447-462 (mut3, Fig. 3c), the main binding epitope in NUT7, did not abolish TAZ2
274 binding in GST-pulldowns, but reduced TAZ2 binding affinity (Fig. 3b, Fig. S3a,b).
275 Additional Alanine substitution of L436, L440, L441 (mut4, Fig. 3c) further reduced TAZ2
276 affinity (Fig. 3b). In contrast, binding was largely abolished by additional mutation to
277 Alanine of L410, L411, Y413, L427, C428, F423, V424, V427, V430 and I431 (mut1, Fig.
278 3b-d, Fig. S3a). As alanine repeat expansion can alter transcription factor condensation
279 properties (Basu et al., 2020), we also generated a NUT variant containing mostly Glycine,
280 Serine and charge reversal mutations (mut2, Fig. 3c). Mut2 also failed to bind TAZ2 in BLI
281 and GST-pulldown experiments (Fig. 3b-d, Fig. S3a).
282
283 As mutation of isolated binding epitopes reduced but did not abolish TAZ2 binding, we
284 conclude that the NUT AD is made up of subdomains that contain short amphipathic
285 interaction motifs that synergise to enable high affinity binding. TF ADs frequently bind
286 p300 through a minimal ΦXXΦΦ motif (X is any residue and Φ is hydrophobic), frequently
287 LXXLL (Plevin et al., 2005). The NUT AD contains several such conserved motifs most of
288 which are predicted to engage TAZ2 (Fig. 3c,e).
289 In our structure, the isolated AD sub-domain in NUT7 is positioned at the interface of the
290 TAZ2 α1, α2 and α3 helices, which frequently functions as a docking site for TF ADs that
291 typically adopt helical structure upon binding (Fig. S3f). AlphaFold (AF) computational
292 models predict 5 helices for NUT (Fig. 3e) that engage the protein interaction surfaces of

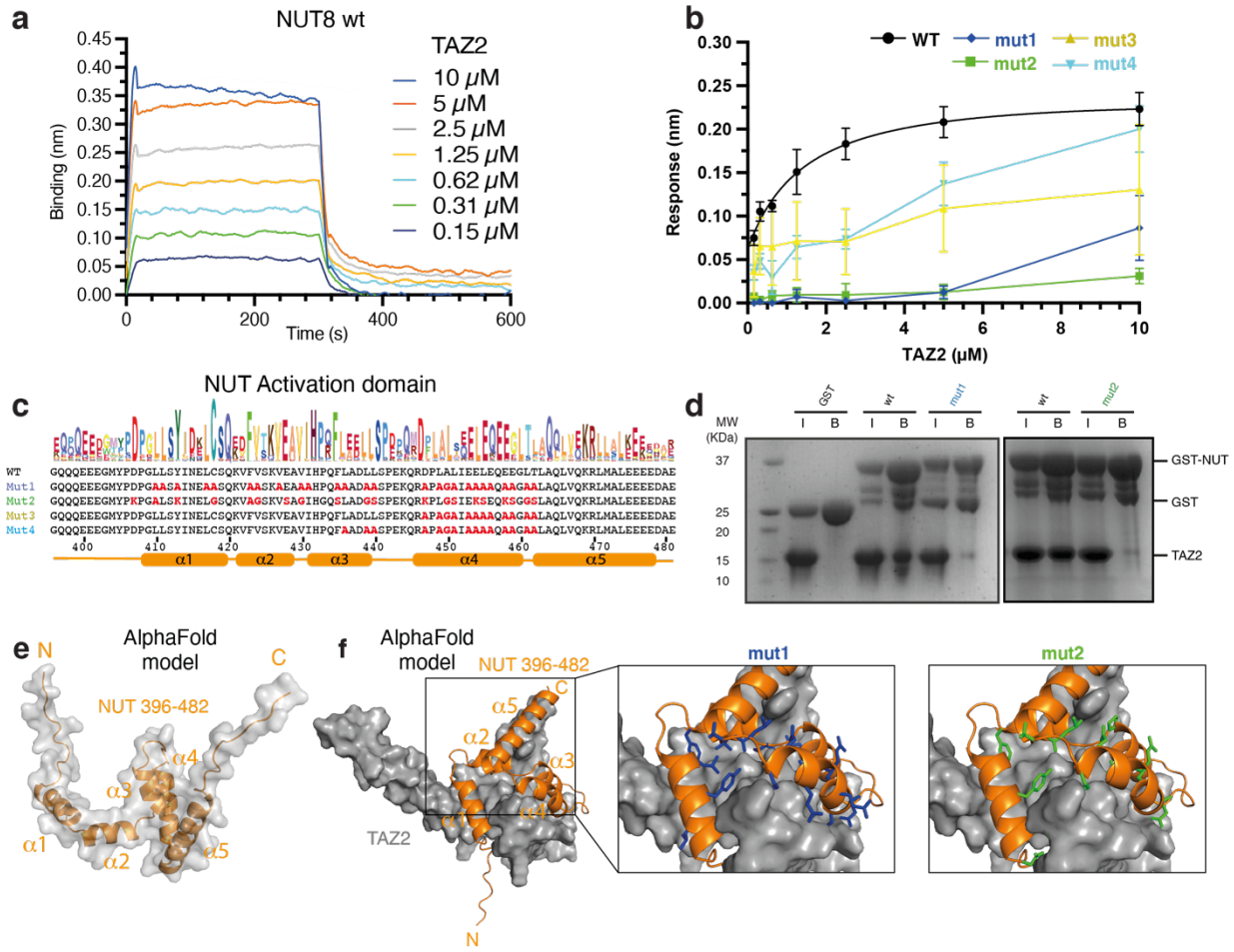

Figure 3. Analysis of the TAZ2-NUT interaction. a, Representative Biolayer Interferometry (BLI) profiles of p300 TAZ2-NUT binding from which the steady-state data were derived. **b**, Steady state analysis of p300 TAZ2 interaction with wild-type and NUT mutants using BLI. Error bars represent the standard deviations from three technical replicate experiments. **c**, Sequences of the NUT AD and mutants (in bold red) used. Top: Skylign plot showing NUT AD sequence conservation; Bottom: predicted secondary structure. **d**, GST pulldown analysis of TAZ2 and NUT8 (396-470) wild type and mutants 1 and 2. **e,** AlphaFold prediction of NUT (396-482) structure. **f**, Left: AlphaFold prediction of the TAZ2-NUT complex structure. Right: mutated residues in NUT mutant 1 (blue) and 2 (green) are shown.

293 TAZ2 (Fig. 3f, Fig. S3c). In the model, the NUT7 AD is re-positioned while the TAZ2 α1,
294 α2, α3 surface is occupied by α3 of the NUT AD. Structure determination of the TAZ2
295 domain in complex with the entire NUT AD was not possible as NMR spectra suffered from
296 severe broadening (data not shown). As (1) isolated AD sub-domains can interact with
297 alternate TAZ2 surfaces (Krois et al., 2016) and (2) as the residues that impair binding are
298 located in the predicted TAZ2-NUT binding interface, we believe this model provides a
299 reasonable starting point for further structural characterization.
300
301 **The role of the TAZ2 domain in p300 regulation and substrate acetylation**
302 Previous data show that NUT stimulates p300 auto- and histone acetylation in cells and *in*
303 *vitro* (Reynoird et al., 2010; Shiota et al., 2018). The AF model of p300 suggests that the
304 TAZ2 domain is positioned over the p300 HAT active site (Fig. S4f, top). The TAZ2 C-
305 terminal helix (amino acids 1806-1836) is sandwiched between the RING and HAT domains
306 proximal to the lysine substrate-binding tunnel in a conformation that is incompatible with
307 substrate access to the HAT active site. In contrast, a model in the presence of NUT AD
308 shows that the TAZ2 domain is displaced from the HAT active site (Fig. S4f, bottom). One
309 possibility is that the TAZ2 domain auto-inhibits the HAT domain and that this auto-
310 inhibition is relieved upon ligand-binding to the TAZ2 domain. As the TAZ2 domain binds
311 numerous transcription factor ADs, such a TAZ2-mediated control mechanism may be
312 broadly relevant and a key aspect of how TFs control chromatin acetylation and gene
313 regulation.
314
315 To test this model, we incubated increasing amounts of GST-NUT8wt with p300s (amino
316 acids 324-2094) in the presence of [^{14}C] acetyl coenzyme A. Addition of NUT WT
317 stimulated p300 auto- and NUT acetylation in a dose-dependent manner (Fig. 4a). Other
318 TAZ2 ligands, Adenoviral E1A or the transcription factor p53 also showed a dose-depended
319 stimulation of p300s auto-acetylation (Fig. 4c,d). In contrast, the TAZ2-binding mutant
320 NUT8mut1 did not show stimulation of p300 auto-acetylation (Fig. 4a). Despite the identical
321 number of lysine amino acids, NUT8mut1 was also not acetylated by p300 (Fig. 4a). These
322 data suggest that the TAZ2 domain autoinhibits p300 activity, possibly through HAT active
323 site restriction (Fig. S4f). Accordingly, acetylation reactions with the core domain of p300
324 (Fig. 1a; p300 core amino acids 1048-1664), lacking TAZ2, show that p300 autoacetylation
325 is not stimulated by the presence of NUT8wt and both NUT8wt and NUT8mut1 substrates
326 are acetylated at equal rates (Fig. 4b). We conclude that the interaction of TF ADs with the
327 TAZ2 domain allosterically regulates p300 HAT activation by relief of autoinhibition.
328
329 Recent data indicate that p300 directly engages nucleosome core particles (NCPs) through its
330 ZZ (Zhang et al., 2018) and TAZ2 domains (Sheahan et al., 2020). Would then TAZ2-
331 engagement also orient NCPs with respect to the HAT active site and specify nucleosome
332 acetylation patterns? In accordance with this possibility, it has been shown that the TAZ2
333 domain is required for efficient acetylation of H3K27, while curbing activity towards other
334 lysine residues within nucleosomes (Sheahan et al., 2020). To test this model, we generated
335 homogeneous 'structure-grade' NCPs as shown by single particle cryoEM (Fig. S4g, Table
336 3). Addition of increasing amounts of NCPs stimulated auto-acetylation of p300s but not
337 p300 core (Fig. 4e). p300 variants containing the TAZ2 domain, as well as the isolated TAZ2
338 domain directly bound to NCPs in EMSA experiments (Fig. 4f, Fig. S4d).
339
340 Cross-linking mass spectrometry experiments showed that surface residues from the p300
341 Bromo-, RING, PHD and TAZ2 domains directly engage the N-terminal regions of Histone
342 H3 and H2A (Fig. 4g, Fig. S4h, Supplementary data). This suggests that NCP engagement by

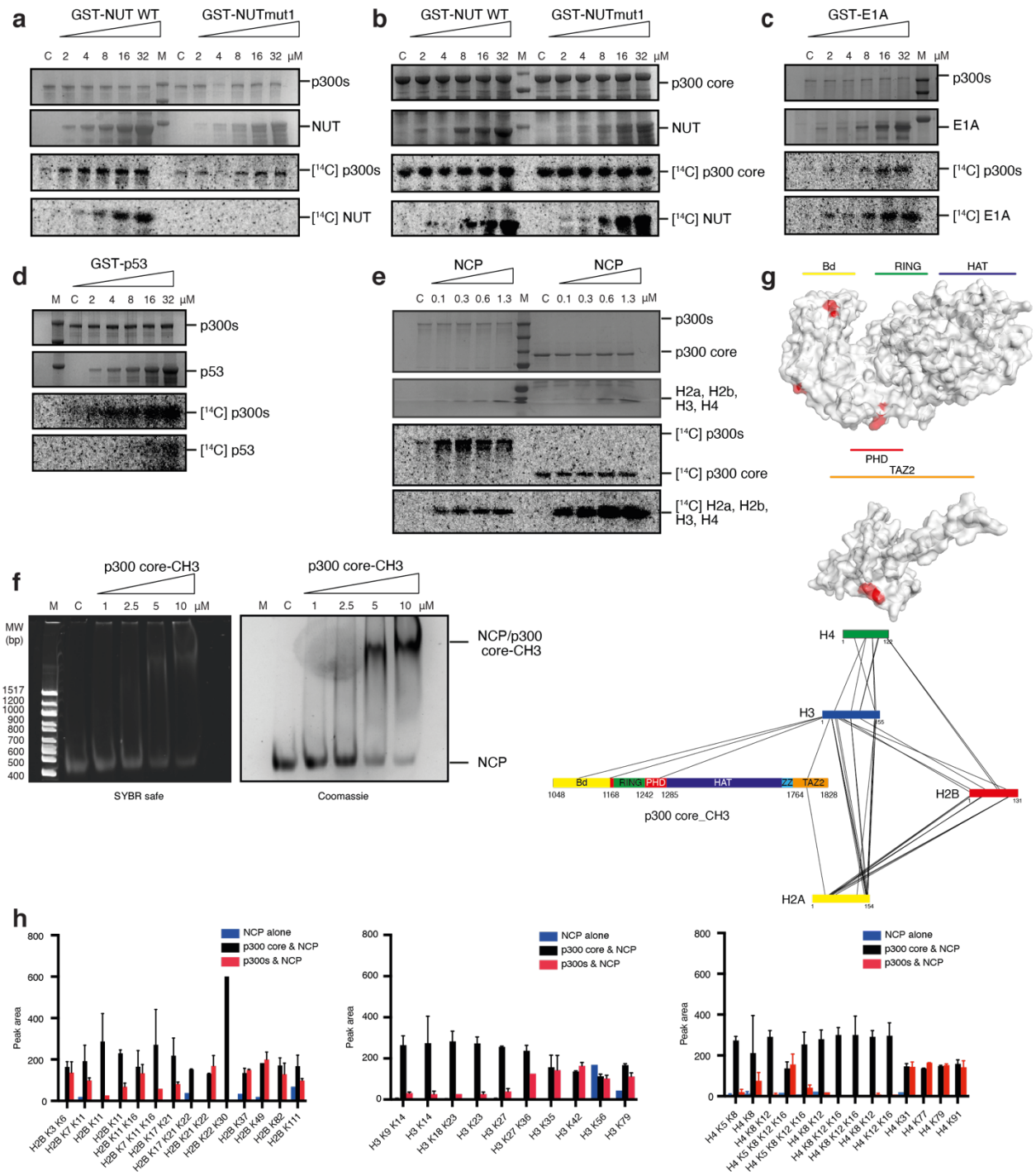

Figure 4. Role of the TAZ2 domain in p300 regulation and substrate acetylation. a, p300s or **b**, p300 core were incubated for with [^{14}C]Acetyl-CoA in the presence or absence (C: p300 alone) of increasing concentrations of NUT8 (396-470) wild type or mutant1, **c**, GST-E1a, **d**, GST-p53 or **e,** NCPs. Top two images: Analysis by SDS–PAGE followed by Coomassie staining and (bottom two images) ^{14}C phosphor imaging. Representative data of three independent experiments are shown. **f**, EMSA analysis of p300 core-CH3 binding to NCPs. Binding reactions were analyzed by native-PAGE and stained with Syber Safe (left) and Coomassie stain (right). **g,** Cross-link (XL-MS) analysis of the p300 core-CH3:NCP complex. Right: Graphical representation of the p300:histone and histones intermolecular cross-links. Left: p300 residues that cross-link to the NCP histones are shown in red on the p300 core (4BHW) and TAZ2 (3IO2) structures. **h**, Quantitative mass spectrometry of NCP acetylation. Reconstituted NCPs were incubated with Acetyl-CoA and p300s or the p300 core. Quantification of the site-specific histone H2B, H3 and H4 acetylation by label-free HPLC/MS/MS. Error bars represent standard deviations from two independent technical replicate experiments.

343 the TAZ2 domain orients the enzyme on NCP substrate. To assess if this interaction
344 contributes to substrate specificity, we assayed NCP acetylation using label free quantitative
345 mass spectrometry. While p300 core, lacking TAZ2, acetylated most lysine residues
346 indiscriminately in Histones H2B, H3 and H4, p300s showed a more selective acetylation
347 pattern thus suggesting that direct NCP binding contributes modestly to substrate specificity
348 (Fig. 4h).
349
350 **Mechanism of condensation of BRD4-NUT and p300**
351 BRD4-NUT forms hyperacetylated chromatin megadomains in patient tumors (Alekseyenko
352 et al., 2015; Reynoird et al., 2010; Rosencrance et al., 2020). Formation of such
353 megadomains can be reproduced by expression of BRD4-NUT in heterologous cell lines
354 (Alekseyenko et al., 2015; Reynoird et al., 2010; Rosencrance et al., 2020). As there is strong
355 evidence that this system reproduces the phenoptype seen in patient cells, we consider it as
356 physiologically relevant, at least with respect to the biophysical properties of the
357 condensation reaction. We generated a series of GFP-BRD4-NUT variants and assessed their
358 propensity to interact with p300 and form co-condensates in the cell nucleus. Co-
359 immunoprecipitation experiments showed that wild-type GFP-BRD4-NUT but not the AD
360 mutants bound to endogenous p300 (Fig. 5a). In agreement with our *in vitro* data, the wild-
361 type but not mutant variants showed a signal at the level of GFP-BRD4-NUT when probed
362 with an anti-acetyl lysine antibody (Fig. 5a). GST-pulldowns in nuclear extracts using a
363 purified GST-NUT8wt fragment showed signal for p300 only for the wild-type but not the
364 AD mutant variants (Fig. 5b). Thus, mutation of the NUT AD interferes with p300 interaction
365 and BRD4-NUT acetylation in cells, as also seen with the corresponding fragments *in vitro*
366 (Fig. 4a).
367
368 Co-transfection experiments showed that GFP-BRD4-NUTwt and RFP-p300 formed nuclear
369 co-condensates (Fig. 5c; row 1; for quantification see Table 4) both in co-transfected and
370 RFP-p300 negative cells. Thus, condensation of GFP-BRD4-NUTwt not only concentrates
371 but also depletes p300 from other areas of the nucleus. These condensates were independent
372 of the NUT AD as mutant variants still formed condensates that co-localized with p300 (Fig.
373 5c; row 2&3) and acetylated chromatin (Fig. S5a). Mutation of the acetyl-lysine binding
374 pocket in BD1 (N140A) and BD2 (N433A) completely abolished GFP-BRD4-NUT and RFP-
375 p300 co-condensation (Fig. 5c; row 4). To assess the model that BRD4 multivalency drives
376 the condensation reaction (Gibson et al., 2019), we mutated BD1 and BD2 individually. We
377 found that mutation of BD1 but not BD2 largely abolished condensation (Fig. 5c; row 5, 6).
378 Thus, the acetyl-lysine binding ability of BD1 is required to nucleate BRD4-NUT and p300
379 co-condensation.
380
381 We reported previously that BRDT interacts with nucleosomes through its first (BD1), but
382 not second (BD2) bromodomain, and that acetylated Histone recognition by BD1 is
383 complemented by a direct BD1–DNA interaction (Miller et al., 2016). Another report
384 indicates that DNA binding promotes condensation of a short BRD4S 'isoform' *in vitro* (Han
385 et al., 2020). We therefore introduced charge inversion mutations in a conserved, basic
386 surface patch in BD1 (R68E, K72E, K76E) that is involved in DNA binding in BRDT (Miller
387 et al., 2016) and in the equivalent BD2 amino acids (S358E, K362E, A366E). Mutation of the
388 basic patch abolished condensation (Fig. 5c; row 7). Thus, we propose that BRD4 BD-DNA
389 interaction facilitates acetylation-dependent NCP binding and chromatin condensation in
390 cells.
391

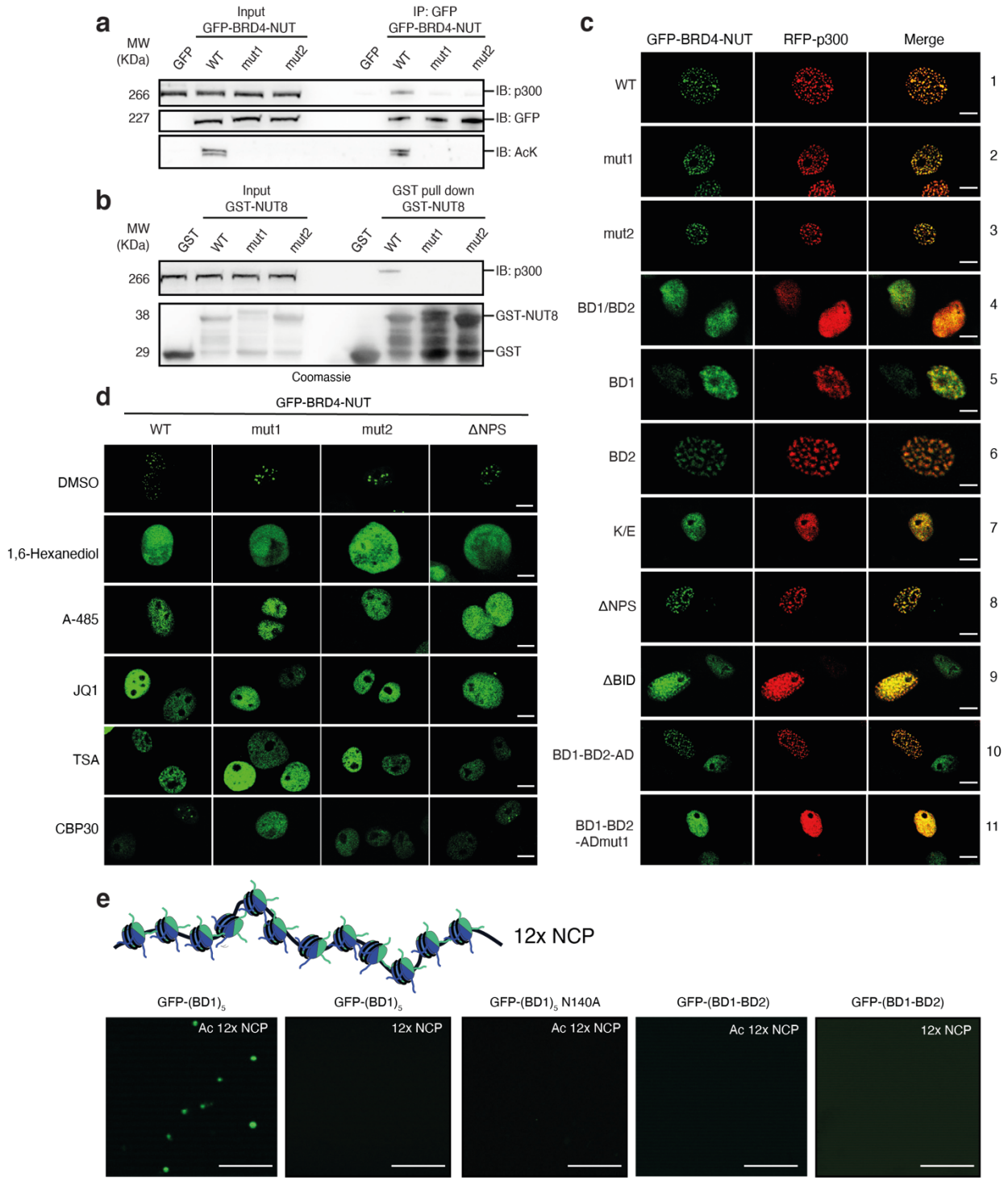

Figure 5. Mechanism of condensation of BRD4-NUT and p300. a, Cos7 cells were transfected with GFP-BRD4-NUT variants or GFP alone as the control. Co-immunoprecipitation (IP) experiments were performed using anti-GFP antibody and immuno-blotted (IB) for p300, GFP and Acetylated-Lysine. Input samples were loaded as a control. Experiments were independently repeated at least three times. **b,** Purified GST-NUT8 wild type and mutants 1 & 2 were incubated with Cos7 cells extract for 4 hours. The complexes were pull-down by Glutathione Sepharose beads and analysed by SDS-PAGE followed by Coomassie staining (bottom) or by IB for p300 (top). **c**, Cos7 cells were transfected with the indicated GFP-BRD4-NUT and RFP-p300 constructs and analysed by fluorescence microscopy, BRD4-NUT (green) and p300 (red). Scale bars, 10 μm. Quantification of foci formation of different BRD4-NUT variants and their co-localization with p300 are shown in Tables 4 and 5. **d**, Cos7 cells were transfected with the indicated GFP-BRD4-NUT constructs and treated with DMSO (control), 1,6-hexanediol, p300 HAT inhibitor A485, pan-BET inhibitor JQ1, HDAC inhibitor TSA or p300 bromodomain inhibitor CBP30. Scale bars, 10 μm. Quantification of foci formation in presence of CBP30 is shown in Table 6. **e**, Reconstituted chromatin containing 12 Nucleosome Core Particles (12x NCP). Fluorescence microscopy images of 12x NCP chromatin templates without and with acetylation by p300 and with GFP-labelled bromodomain-containing proteins. Scale bars, 10 μm.

392 We also probed the BRD4 N-terminal cluster of phosphorylation sites (NPS) and the basic
393 residue-enriched interaction domain (BID), elements that have been proposed to enable
394 BRD4 regulation by phosphorylation (Wu et al., 2013). Deletion of the NPS did not interfere
395 with condensation while removal of the BID reduced condensation (Fig. 5c; row 8, 9). A
396 minimal BD1-BD2 variant fused to the AD but not an AD Mut1 variant (Fig. 1b) still formed
397 p300 co-condensates (Fig. 5c; row 10, 11, Movie S1). The BD1-BD2-AD fusion protein but
398 not the AD Mut1 variant was still able to co-IP p300 from cells indicating that the ability to
399 interact with p300 is maintained in the fusion protein (Fig. S5c). We therefore conclude that,
400 at a minimal level, both BRD4 BD acetyl-lysine binding and p300 recruitment are required
401 for condensation.
402
403 Addition of 1,6-hexanediol, the p300/CBP HAT inhibitor A-485 or the BET inhibitor JQ1 all
404 abolished condensation of GFP-BRD4-NUTwt, mut1, mut2 and ΔNPS confirming that both
405 acetylation by p300/CBP and BRD4 BD substrate engagement are required (Fig. 5d, Table
406 6). HDAC inhibition results in expansion of Histone acetylation and retargets lysine-acetyl
407 readers including BRD4 thus partially mimicking the effect of BD inhibition (Slaughter et al.,
408 2021). In agreement with this model, addition of the HDAC inhibitor Trichostatin A
409 abolished condensation of all variants (Fig. 5d). Immunofluorescence experiments further
410 showed that the BRD4-NUT condensates colocalise with HDAC1 thus confirming that these
411 sites correspond to high acetylation turnover (Fig. S5b).
412
413 As mutation of the NUT AD does not abolish p300 recruitment into the condensate we
414 further assessed the contribution of the CBP/p300 BD. We used the CBP30 inhibitor that
415 has~34-fold higher selectivity for CBP/p300 BD as compared to BRD4 BD1 (Hammitzsch et
416 al., 2015). Addition of CBP30 did not impact the condensation of GFP-BRD4-NUTwt and
417 ΔNPS. However, condensation of the NUT AD mutants GFP-BRD4-NUTmut1 and mut2 was
418 sensitive to CBP30 treatment (Fig. 5d, Table 7). Thus, the NUT AD mutants reveal that co-
419 condensation can also occur through a p300 BD-acetyl-lysine-dependent recruitment
420 mechanism. Thus, two interactions drive BRD4-NUT and p300 co-condensation: (1)
421 interaction of p300 with the AD domain in NUT and (2) p300 BD-acetyl-lysine engagement.
422 Disruption of both interactions, but not each interaction individually, abolishes the co-
423 condensation reaction.
424
425 **Condensation requires BD oligomerization**
426 Our observation that mutation of BD1 but not BD2 largely abolished BRD4-NUT
427 condensation in cells (Fig. 5c; row 5, 6) suggests that condensation in cells is not simply
428 driven by BRD4 BD divalency. We therefore tested the requirements of acetylation-
429 dependent chromatin condensation *in vitro*. Previous data show that addition of BRD4 or an
430 engineered multivalent protein containing five copies $(BD1)_5$ of BRD4 BD1 induces
431 condensation of p300-acetylated nucleosome arrays *in vitro* (Gibson et al., 2019).
432 Condensation in this *in vitro* system depends on BD acetyl-lysine binding and multivalency
433 (Gibson et al., 2019).
434
435 We generated dodecameric nucleosome arrays (Fig. 5e, Fig. S5d). In agreement with
436 previous data (Gibson et al., 2019), non-acetylated nucleosome arrays formed round droplets
437 that were dissolved by p300 acetylation (Fig. S5e), in agreement with the model that
438 acetylation disrupts internucleosomal interactions (Shogren-Knaak et al., 2006). As expected,
439 addition of GFP-$(BD1)_5$ allowed droplet formation of acetylated but not of non-acetylated
440 nucleosome arrays (Fig. 5e). This condensation reaction was driven by BD1-acetyl-lysine

441 binding as a N140A mutation in the acetyl-lysine binding pocket abolished droplet formation
442 (Fig. 5e, middle).
443
444 As a minimal BRD4 construct containing BD1-BD2 (amino acids 1-459) induced
445 condensation in cells when fused to the NUT AD, we tested if BD1-BD2 divalency is
446 sufficient to drive droplet formation *in vitro*. However, we found that BD1-BD2 did not
447 enable droplet formation of acetylated or non-acetylated nucleosome arrays (Fig. 5e, right).
448 As a consequence, mutation of the BD acetyl-lysine binding pockets (BD1 N140A-BD2;
449 BD1-BD2 N433A or BD1 N140A -BD2 N433A) also did not have impact droplet formation
450 under these conditions (Fig. S5f). We conclude that the BD divalency of BRD4 is not
451 sufficient to drive condensation *in vitro*. As large-scale condensation in cells is sensitive to
452 BD1 but not BD2 mutation (Fig. 5c), our model is that multivalency is established by BRD4
453 oligomerisation.
454
455 **Dynamics of condensation of BRD4-NUT and p300**
456 Time-lapse imaging showed that the condensates remained stable during the experiment (Fig.
457 6a, Movie S2). Addition of 1,6-hexanediol resulted in rapid and transient dissolution of the
458 condensate (Fig. 6b). After reformation, a second addition of 1,6-hexanediol dissolved the
459 condensates again illustrating their dynamic and transient nature. To study the consequences
460 of the BRD4-NUT mutations on turnover of the condensate we performed Fluorescence
461 Recovery After Photobleaching (FRAP) experiments. Wild-type GFP-BRD4-NUT and RFP-
462 p300 recovered ~50% of signal after ~20 sec (Fig. 6c). Thus, while droplets appear stable at
463 the mesoscale, the molecules are highly mobile at the nanoscale and in constant exchange
464 with the nucleoplasm. Mutation of BRD4-NUT mostly interfered with droplet retention as
465 shown by increased FRAP recovery rates (Fig. 6d). p300 dynamics was directly coupled to
466 that of the BRD4-NUT mutants except for the GFP-BRD4-NUT BD2 and the BD1-BD2-AD
467 constructs which showed slower p300 recovery rates indicating some degree of functional
468 uncoupling.
469
470 To assay internal droplet dynamics, we performed half-bleach FRAP experiments (Fig. 6e).
471 We analysed the change in fluorescence intensity over time along a defined A-B axis in the
472 bleached (red square) and unbleached area. Kymograph analysis showed that the
473 fluorescence signal in the 'unbleached' region (orange line) and the droplet 'center' (blue
474 line) recovered much quicker and to completion as compared to the 'periphery' of the droplet
475 (grey line), which only partially recovered signal (Fig. 6f). Our interpretation is that recovery
476 at the center occurs more quickly because high local concentration in the droplet center
477 maintains a feed-forward acetylation reaction that traps quickly diffusing molecules. At the
478 droplet periphery, lower concentrations and competition with HDACs destabilizes droplet
479 assembly leading to reduced recovery rates. As there is (1) constant exchange with the
480 nucleoplasm and (2) no preferential equilibration between the bleached and unbleached area
481 we argue that these condensates are 'liquid'-like at the nanoscale but not at the mesoscale
482 where the viscoelastic properties of the 'solid' chromatin scaffold constrain dynamic
483 exchange (Strickfaden et al., 2020). As a result, we do not see droplet fission or fusion at
484 least during the time-course of our experiments.
485
486 **Discussion**
487 Chromatin acetylation has long been linked to transcriptional activation, by altering
488 chromatin structure and by enabling binding of BD containing proteins (Dhalluin et al., 1999;
489 Eberharter and Becker, 2002; Strahl and Allis, 2000). How acetylation promotes transcription
490 has remained elusive. p300 is responsible for up to a third of nuclear acetylation (Weinert et

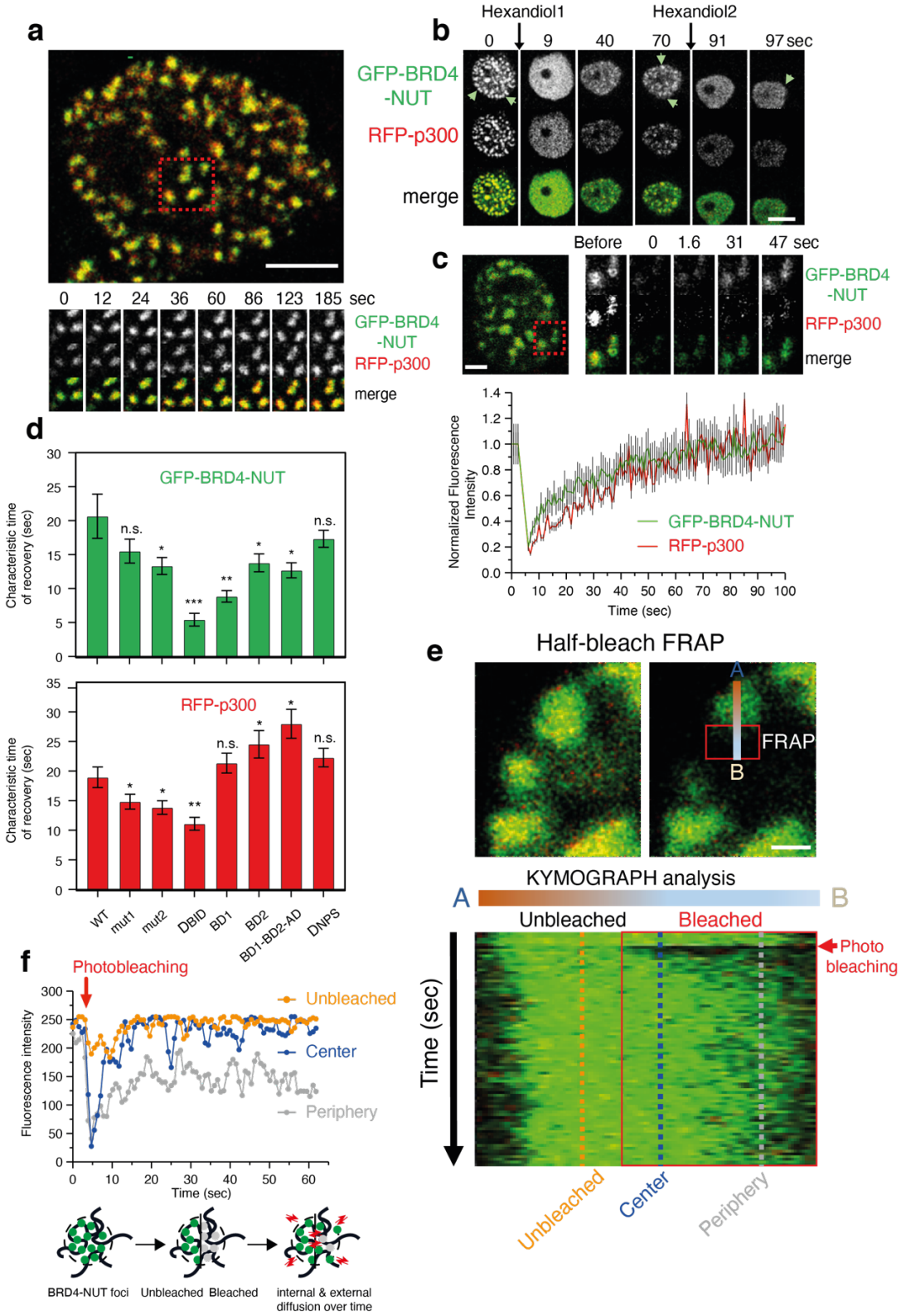

Figure 6. Dynamics of condensation of BRD4-NUT and p300. a, Example image of nuclear droplets. Red square: Time laps imaging of BRD4-NUT and p300 droplets; Scale bar, 4 µm. **b,** Time laps imaging after addition of 3% [w/v] 1,6 Hexanediol. Scale bar, 12 µm. **c**, Top: Example image of droplets (red square) after photobleaching. Scale bar, 2 µm. Bottom: Quantification of the FRAP experiments. 3 independent technical replicates were done. Averages and standard error of mean (SEM; grey bars) are shown. **d**, Quantification of the characteristic time of recovery rates for different GFP-BRD4-NUT mutants (top) and RFP-p300 (bottom). Three to four technical replicate FRAP experiments were done for each mutant (40 to 65 foci measured). Data shown are mean +/-standard error of mean (SEM). Statistical differences in recovery rates were determined by Student's t-test. *p≤0.05; **p≤0.01; ***p≤0.001; n.s. non-significant difference as compared to WT. **e**, Half-bleach FRAP experiment. Top: The area before (left) and after (right) laser bleach are shown. The red box indicates the bleached area. Scale bar, 0.5 µm. Bottom: The change in fluorescence intensity along the A-B axis was analysed in the Kymograph. **f**, Top: Plot of fluorescence recovery from the Kymograph for the unbleached area, center and periphery of the droplet. Bottom: cartoon of the internal and external exchange.

491 al., 2018). The BRD4-NUT fusion reveals how constitutive activation of p300 establishes a
492 self-organizing, acetylation-dependent feed-forward reaction that results in large-scale intra-
493 and interchromosomal interactions with an oncogenic outcome (Eagen and French, 2021). In
494 addition to its well-known role in enhancer function and control of gene expression (Ma et
495 al., 2021; Narita et al., 2021), p300 is also involved in compartmentalisation of the genome
496 into eu- and heterochromatin (Cabianca et al., 2019). We argue that key aspects of these
497 reactions involve modulation of an acetylation-dependent condensation reaction we describe
498 here.
499
500 Regulation of p300 is central for establishment of such acetylation-dependent condensation
501 reactions (Fig. 7a). We propose that in the deacetylated state p300 is auto-inhibited by the
502 RING, TAZ2 domains and the AIL. p300 is activated by trans-autoacetylation (Karanam et
503 al., 2006; Ortega et al., 2018; Thompson et al., 2004). Due to low p300 concentration
504 (Gillespie et al., 2020), self-collision and activation do not occur spontaneously. Instead, as
505 HDACs are estimated to be ~100-fold more abundant (Gillespie et al., 2020), p300 most
506 frequently collides with HDAC complexes (Black et al., 2008; Hogg et al., 2021) which
507 maintain p300 in the inactive conformation. In this inactive state p300 is evenly dispersed in
508 the nucleus (Ortega et al., 2018).
509
510 Induced proximity, by TF binding, enables p300 self-collision, trans-autoacetylation and
511 activation (Ortega et al., 2018). The BRD4-NUT system reveals an autoinhibitory role for the
512 TAZ2 domain which is relieved upon NUT AD binding (Fig. 4). Accordingly, other well-
513 characterized TAZ2 ligands including the ADs of E1A and p53 (Hsu et al., 2018; Krois et al.,
514 2016; Pelka et al., 2009) also stimulate p300 auto- and substrate acetylation (Fig. 4), as also
515 reported for other TAZ2 ligands (Hansson et al., 2009; Kraus et al., 1999). Thus, we propose
516 that the TAZ2 domain plays a role in allosteric HAT regulation: TF AD binding results in
517 displacement of the TAZ2 domain from its auto-inhibitory position resulting in HAT
518 activation thus directly coupling TF AD-mediated p300 binding to HAT activation (Fig. S4f).
519
520 Perturbation of the autoinhibitory function of the RING and TAZ2 domains by mutation all
521 lead to constitutive p300 activation and condensation reactions similar to what is seen with
522 BRD4-NUT (Delvecchio et al., 2013; Ortega et al., 2018). Importantly, comprehensive
523 studies of cancer cell lines show that truncation of the C-terminal helix of TAZ2, which we
524 predict is required to stabilise the autoinhibitory conformation (Fig. S4f), also lead to p300
525 HAT gain-of-function in disease (Ghandi et al., 2019; Kumar et al., 2021). An acetylation-
526 dependent condensation reaction may also explain how Adenoviral E1A causes genome-wide
527 relocalisation of p300 and activation of genes that promote cell growth and division (Ferrari
528 et al., 2014; Ferrari et al., 2008; Horwitz et al., 2008). Not unlike BRD4-NUT, this
529 condensation reaction is also sensitive to p300 HAT, BD and HDAC inhibition (Ferrari et al.,
530 2014). Therefore, while p300 is thought of as a classic tumor suppressor, with loss of
531 function mutations occurring in a number of different cancers (Attar and Kurdistani, 2017),
532 constitutive activation by mutation or by interaction with activating ligands such as BRD4-
533 NUT and E1A can lead to acetylation-dependent condensation with an oncogenic outcome.
534
535 As numerous TFs interact with p300 trough their ADs (Dyson and Wright, 2016; Goodman
536 and Smolik, 2000), we predict that the condensation reaction establishes intra- and
537 interchromosomal interactions that are normally involved in enhancer signaling (Fig. 7b).
538 Many TF ADs, including NUT (Fig. 1), are IDRs that form dynamic interactions with the
539 different protein interaction domains of p300 (Dames et al., 2002; Feng et al., 2009; Ferreon
540 et al., 2009; He et al., 2011; Krois et al., 2016; Lee et al., 2010; Marceau et al., 2019; Miller

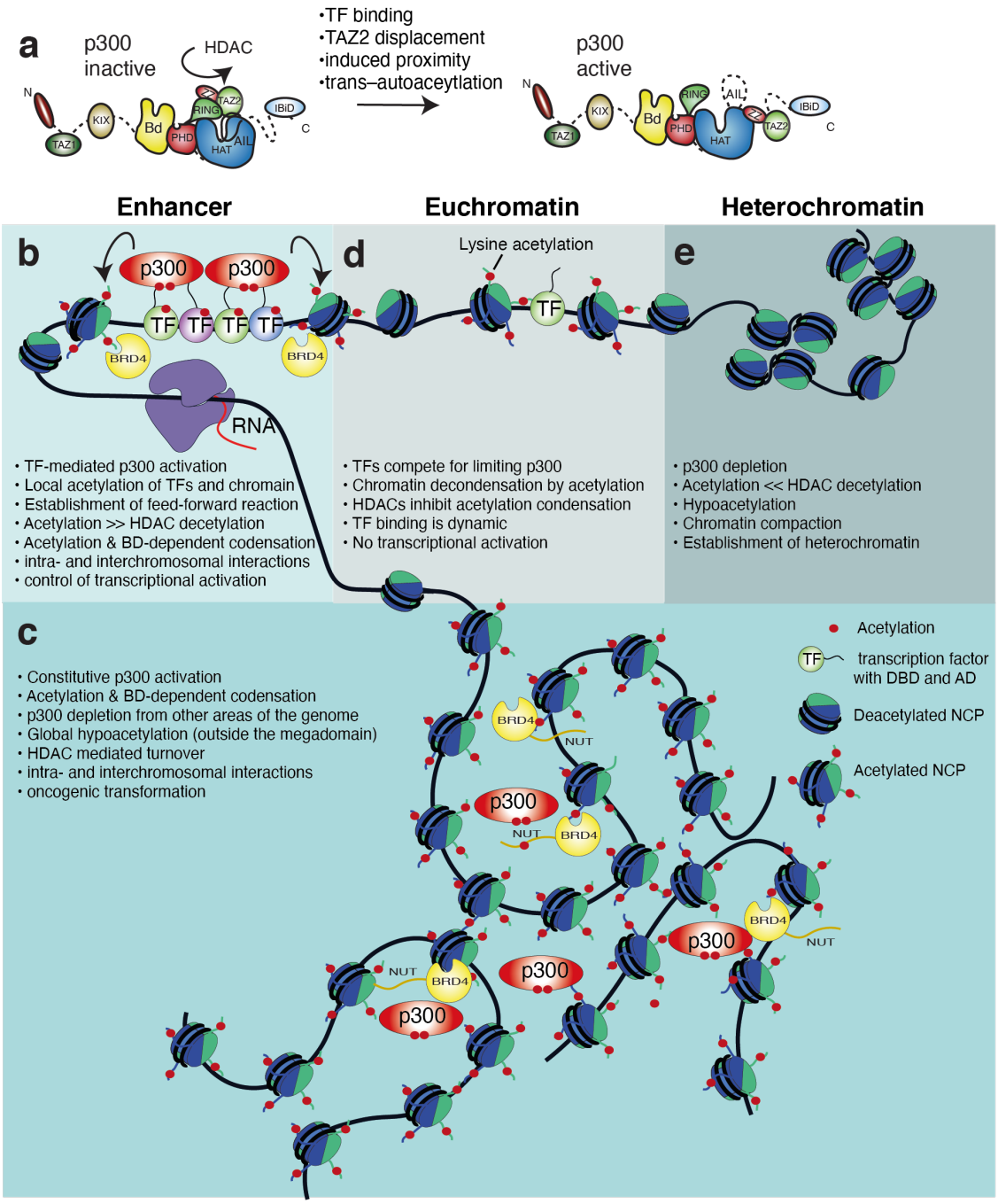

Figure 7. Molecular model for p300 activation in physiological setting and disease. **a**, p300 is maintained in the inactive state by HDACs. Activation requires TF binding which results autoacetylation and removal of autoinhibition. **b,** In enhancer signalling, TFs interact through their ADs with the different protein interaction domains of p300 which results in scaffolding of dynamic TF assemblies. Local TF and histone acetylation allows binding of BD containing proteins including BRD4 thus establishing positive feed-back. HDACs are located in these condensates and enable dynamic turnover thus resulting in bistability and response to changes in TF signaling. **c,** In BRD4-NUT NMC, the acetylation-dependent reaction drives formation of intra- and interchromosomal interactions resulting in the formation of a Megadomain. **d,** TF binding and acetylation establish open Euchromatin. TFs compete for limiting p300 co-activators but TF-DNA binding outside enhancer clusters remains transient and, due to high HDAC activity, does not effectively establish an acetylation-dependent condensate. **e,** Depletion and partitioning of p300 into euchromatic compartments results in hypoacetylation due to high HDAC activity. Hypoacetylated compartments become a substrate for heterochromatinization.

541 Jenkins et al., 2015; Mukherjee et al., 2013; Wang et al., 2012a; Wojciak et al., 2009). Due to
542 such multivalent AD interactions, p300 is able to scaffold TF assembly on complex enhancer
543 elements thereby facilitating combinatorial control of enhancer-mediated transcription (Chan
544 and La Thangue, 2001; Panne, 2008; Panne et al., 2007).
545
546 TF-mediated recruitment and activation of p300 result in local histone and TF acetylation and
547 establishment of positive feed-back through binding by BD containing proteins. High rates of
548 self-collision of p300 maintain this positive feedback and establish a self-organizing feed-
549 forward reaction resulting in co-condensation of p300, BET proteins BRD2, BRD3, and
550 BRD4 and numerous transcriptional and chromatin regulators, which are all present in
551 BRD4-NUT condensates (Alekseyenko et al., 2017). The condensation reaction is limited by
552 HDACs which are usually present at active enhancers and promoters (Wang et al., 2009;
553 Whyte et al., 2012), and prevent hyperacetylation and transcriptional inhibition (Gryder et al.,
554 2019a; Gryder et al., 2019b). HDAC1 is localised in the BRD4-NUT condensate (Fig. S5b).
555 Our FRAP experiments show that the condensates are 'liquid'-like at the nanoscale and we
556 propose that HDACs enable continuous and dynamic turnover. If the feed-forward
557 condensation reaction is sufficiently strong, it will overcome this inhibitory effect by HDACs
558 provided that local high concentrations are maintained. As a result, the BRD4-NUT
559 condensate is essentially stable at the mesoscale despite continuous internal dynamic
560 exchange. In enhancer signaling, this dynamic bistability may then render the condensate
561 more immediately responsive to dynamic and transient changes in TF signaling and explain
562 the short transcriptional burst kinetics seen in cells (Fukaya et al., 2016; Li et al., 2019).
563
564 The reaction redistributes p300 (and BD containing proteins) into the condensate thus leading
565 to depletion from other genomic regions (Fig. 5) (Reynoird et al., 2010). The condensation
566 reaction thus leads to high local acetylation (in the condensate) but global histone
567 hypoacetylation elsewhere (Schwartz et al., 2011). Counterintuitively, treatment with HDAC
568 inhibitors does not lead to BRD4-NUT 'hypercondensation'. Instead, HDACi restores global
569 histone acetylation (Schwartz et al., 2011) and rapidly dissolves the BRD4-NUT/p300
570 condensate (Fig. 5). In agreement with recent data (Slaughter et al., 2021), our model is that
571 HDAC inhibition and resultant increased global histone acetylation redistributes BD
572 containing proteins thereby decreasing their effective local concentration resulting in droplet
573 dissolution. Due to the diffusible nature of the reactants, maintenance of global histone
574 hypoacetylation is therefore a key aspect of how such condensates arise. We therefore argue
575 that HDACs contribute to transcriptional regulation by maintaining (1) dynamic bistability of
576 enhancer condensates and (2) global hypoacetylation which in turn 'enables' focal enhancer
577 condensation. Thus, the dual nature of HDAC function with roles in gene activation and
578 repression (Kidder and Palmer, 2012; Rundlett et al., 1996; Vogelauer et al., 2000; Wang et
579 al., 2009) would then be directly linked to modulation of these condensation reactions.
580
581 While histone H3K27 acetylation has long been seen as a signature mark for active enhancers
582 (Creyghton et al., 2010; Rada-Iglesias et al., 2010), p300 also acetylates numerous non-
583 histone substrates including many TFs (Fig. 4) (Weinert et al., 2018). Therefore, we do not
584 see a role for a defined 'code' in how such modifications contribute to the signalling reaction
585 (Zhang et al., 2020). Instead, promiscuous lysine acetylation of TFs and histones drive
586 emergent multivalency that kinetically traps diffusing BD-domain containing factors such as
587 p300 and BRD4. While individual BDs typically have weak binding affinity and specificity
588 (Filippakopoulos and Knapp, 2012), local proximity facilitates rebinding after dissociation
589 thus enabling an acetylation-dependent feed-forward co-condensation reaction (Fig. 6). We
590 propose that this biophysical mechanism enables formation of an 'exploratory' network of

interactions that generates bistability by positive feedback and enables focal accumulation of regulatory factors on enhancers and establishment of long-range interactions that control promoter activity (Li et al., 2019). Successful establishment of this 'exploratory' network could then explain the long-standing observation that multiple TF DNA binding sites synergistically activate transcription without the requirement of physical interaction between TFs (Carey et al., 1990; Panne et al., 2007).

It has long-been known that TFs activate some genes while at the same time repressing others through competitive coactivator 'squelching' (De Bosscher et al., 2003; Gill and Ptashne, 1988; Guertin et al., 2014; Hottiger et al., 1998; Kamei et al., 1996; Meyer et al., 1989; Portuguez et al., 2019; Triezenberg et al., 1988). Accordingly, in BRD4-NUT, the sequestration of p300 inhibits p53 and the apoptotic cell response while knock-down of BRD4-NUT releases p300, and restores p53-dependent cell differentiation and apoptosis (Reynoird et al., 2010). Thus, we predict that competition for diffusible co-activators and successful establishment of a continual acetylation-dependent condensation reaction is a key regulatory control mechanism: only enhancers containing the appropriate set of clustered TF binding sites will effectively compete in establishing such an acetylation-dependent condensate. Due to high concentrations of HDACs (Gillespie et al., 2020) and rapid deacetylation kinetics across the genome (Hogg et al., 2021; Weinert et al., 2018), the acetylation-dependent condensation reaction is transient. It is such transient and dynamic acetylation that establishes euchromatic compartments without necessarily leading to transcriptional activation (Fig. 7d).

There is increasing evidence suggesting a role for LLPS of intrinsically disordered proteins in different nuclear processes (Han et al., 2020; Sabari et al., 2018; Shin et al., 2018). IDR-driven condensation reactions of chromatin-binding proteins including BRD4 and p300 have been implicated in gene regulation (Boija et al., 2018; Chong et al., 2018; Guo et al., 2019; Han et al., 2020; Ma et al., 2021; Sabari et al., 2018; Shin et al., 2018; Zamudio et al., 2019) and in disease (Ahn et al., 2021; Boija et al., 2021). As BRD4-NUT and p300 are largely disordered (Fig. 1; 72% and 42% predicted IDR, respectively) our assumption was that IDR-mediated interactions would contribute to the condensation reaction.

While the NUT AD region can indeed form spherical condensates *in vitro* as analysed by SAXS (Fig. S6b,c), we do not think that this is relevant for the condensation reaction in cells. Even a minimal BRD4 BD1-BD2 construct, removing a large fraction of IDR sequence from BRD4-NUT, enables condensation in cells provided it contains a functional AD (Fig. 5c). As an equivalent NUT AD mutant (that fails to bind to the TAZ2 domain) does not enable the condensation we exclude the possibility that residual structural disorder, e.g. the 200 amino acid linker between the BD1 and BD2 domains of BRD4, drives the condensation reaction. We and others have shown that the condensation reaction is inhibited by (1) the BET BD inhibitor JQ1 (Reynoird et al., 2010; Wang and You, 2015), (2) mutation of the acetyl-lysine binding pocket of BRD4 BD1 or, (3) the DNA binding surfaces of BRD4 BD1/BD2 or, (4) p300 HAT inhibition (Fig. 5). In addition, several p300 HAT gain-of-function mutations, that interfere with the autoinhibitory function of the RING and TAZ2 domains, enable a similar acetylation- and BD-dependent condensation reaction (Ortega et al., 2018). We therefore conclude that the reaction is driven by p300 activation and engagement of acetylated chromatin by the BDs. In accordance, single-gene imaging data support the notion that promoter-enhancer communication and transcription control depend on TF and BRD4 clustering driven by specific DNA and BD binding rather than IDR-mediated interactions (Li et al., 2020).

641
642 Further, as (1) divalent BD1-BD2 did not enable condensation of acetylated nucleosome
643 arrays *in vitro* (Fig. 5), and (2) as of mutation of BRD4 BD1 is sufficient to abolish
644 condensation in cells, our model is that the condensate does not arise due to BRD4 BD1-BD2
645 divalency. Instead, as BET proteins form higher-order oligomers on acetylated chromatin
646 (Pivot-Pajot et al., 2003; Wang et al., 2012b), our model is that BD-mediated oligomerisation
647 and emergent multivalency drive condensation.
648
649 TFs locate their target DNA sites using 'facilitated diffusion' (Halford, 2009; Mirny et al.,
650 2009). We propose that following TF-DNA binding, the combined action of p300
651 scaffolding, TF acetylation and formation of an acetylation-dependent condensate slows
652 down the dynamic search behaviour thus increasing local concentration, residency time and
653 transcription activation. Accordingly, acetylation-mediated increase of TF residence time has
654 been described for p53 (Loffreda et al., 2017; Luo et al., 2004) and could thus control TF
655 turnover and transcriptional regulation (Gurdon et al., 2020; Lickwar et al., 2012). Binding
656 events that occur outside TF enhancer clusters are then unable to compete for limited co-
657 activators and fail to establish such an acetylation-condensation reaction and therefore remain
658 largely dynamic and transcriptionally inactive (Fisher et al., 2012; Kribelbauer et al., 2019; Li
659 et al., 2008).
660
661 The co-activator depletion reaction may also be one of the key reaction mechanisms that
662 enables the physical segregation of transcriptionally active euchromatin from repressed
663 heterochromatin (Fig. 7e), and explain the general link between the transcriptional state and
664 3D chromatin compartmentalisation (Rowley and Corces, 2018). Targeting of
665 heterochromatin with acidic TF ADs or treatment with HDAC inhibitors generally
666 counteracts heterochromatinization even in the absence of active transcription (Ahmad and
667 Henikoff, 2001; Aparicio and Gottschling, 1994; Carpenter et al., 2005; Chambeyron and
668 Bickmore, 2004; Mueller et al., 2001; Taddei et al., 2001; Therizols et al., 2014; Toth et al.,
669 2004; Tumbar et al., 1999a; Tumbar et al., 1999b). TF-mediated retention of p300 in
670 euchromatin enables establishment of heterochromatin in worms (Cabianca et al., 2019),
671 while depletion of p300 and chromatin hypoacetylation facilitates methylation by PRC2
672 (Hogg et al., 2021). Thus, competition for and partitioning of limiting key acetylases by TFs
673 into euchromatin and depletion from heterochromatin, together with BD-mediated higher
674 order chromatin folding (Gaucher et al., 2012; Pivot-Pajot et al., 2003; Wang et al., 2012b),
675 may drive key aspects of 'epigenetic' genome compartmentalization. Phenomena such as
676 stochastic and exclusive choice of monoallelic gene expression or X-chromosome
677 inactivation in mammals may then also depend on depletion of limiting coactivators and
678 establishment of positive feedback so that only the 'winning' allele drives gene expression
679 while 'competing' alleles are silenced (Apostolou and Thanos, 2008; Jeppesen and Turner,
680 1993; Monahan et al., 2019; Spilianakis et al., 2005; Zylicz et al., 2019).
681
682 **Methods**
683
684 **Constructs.** cDNA encoding residues for NUT-F1c (347-588), NUT1 (347-446), NUT2 (427-527),
685 NUT3 (508-588), NUT4 (347-480), NUT5 (347-514), NUT6 (351-470), NUT7 (448-492) (wild type
686 and mutants), NUT8 (424-492) (wild type and mutants), NUT9 (395-482) and p53 (1-61) were cloned
687 into the *Nco*I/*Xho*I restriction sites of vectors pETM-30 or pETM11 (EMBL) with a tobacco etch
688 virus (TEV)-cleavable N-terminal His_6 glutathione S-transferase (His_6-GST) tag for pETM30 or an N-
689 terminal His_6-tag for pETM11. The p300 TAZ2 domain constructs (TAZ2 1723-1812, TAZ2 1723-
690 1822, TAZ2 1723-1836) were codon optimized and cloned into the *Nco*I/*BamH*I restriction sites of

691 pETM-11 (EMBL) with a TEV-cleavable N-terminal His_6-tag. Cysteines which do not participate in
692 zinc coordination were mutated to Alanine or Serine (C1738, C1746, C1769, C1770). The CH3
693 domain of p300 (1660-1815) was cloned using *EcoR*I/*Xho*I restriction sites in pGEX-5X1 vector with
694 a TEV-cleavable N-terminal glutathione S-transferase (GST) tag. p300s (324-2094) and p300 core-
695 CH3 (1043-1828 and 1043-1817) were produced as described previously (Delvecchio et al., 2013).
696 The BRD4 constructs: GFP-BD1-BD2, GFP-BD1-BD2 N140A/N433A, GFP-BD1-BD2 N140A and
697 GFP-BD1-BD2 N433A were cloned into the *Nco*I/*Xho*I restriction sites of pETM11. The vectors
698 expressing the GFP-(Bromo)5 and the GFP-(Bromo)5 N140A were gifts from Michael Rosen lab
699 (University of Texas Southwestern). The co-expression vector encoding the *S. cerevisiae* histones was
700 a gift from Stephen Harrison lab (Harvard Medical school). The vector expressing the E1A protein
701 was a gift from Andy Turnell lab (University of Birmingham). For cell-based assays, all the GFP-
702 tagged BRD4-NUT variants (Table 2), RFP-tagged NUT-F1c, NUT1, NUT2, NUT3 and NUT4 and
703 RFP tagged p300 were cloned into pEGFP-C1 vector (Clontech). All constructs were confirmed by
704 DNA sequencing.
705
706 **Expression and purification.** Expression and purification of Flag-tagged p300s and GST-tagged
707 p300 core-CH3 constructs was done as reported previously (Delvecchio et al., 2013; Ortega et al.,
708 2018). All p300 TAZ2 constructs were produced as inclusion bodies in *Escherichia coli* (*E. coli)*
709 BL21 (DE3). Cells were grown to mid-log phase (OD600 ~ 0.6) at 37°C in Luria Broth containing 50
710 µg/ml kamamycin and 200 µM $ZnSO_4$. Protein expression was induced by addition of 1 mM
711 isopropyl-β-D-thiogalactopyranoside (IPTG) at 18°C for 16h. Uniformly ^{15}N- and $^{15}N/^{13}C$-labelled
712 samples were produced from cells grown in M9 minimal medium containing 50 µg/ml Kanamycin,
713 200 µM $ZnSO_4$ and 1 g/l of $^{15}NH_4Cl$ and 2g/l ^{13}C glucose. Cells were harvested by centrifugation for
714 20 mins at 5000 g in a SLC-6000 rotor (Sorvall) and resuspended in 50 ml/L culture lysis buffer 1 (20
715 mM Tris-HCl pH 7.5, 300 mM NaCl, 5 µM $ZnSO_4$, 1 mM Dithiothreitol (DTT)), supplemented with
716 EDTA-free protease inhibitors (Roche), and 10 µl of benzonase nuclease (Sigma-Aldrich). Cells were
717 sonicated and centrifuged in a SS-34 rotor (Sorvall) for 1h at 12000 rpm. The pellet was then washed
718 three times in the lysis buffer and the final pellet resuspended in buffer 2 (20 mM Tris pH 7.5, 300
719 mM NaCl, 1 mM Dithiothreitol (DTT), 6 M urea) for one hour at 4 °C on a rotating device. The
720 protein solution was centrifuged as above and the soluble fraction applied to Ni^{2+}-charged IMAC
721 Sepharose 6 FF (Cytiva) beads preequilibrated with buffer 2 containing 20 mM Imidazole. The
722 column was washed with 20 column volumes (CVs) of buffer 2 containing 20 mM Imidazole and the
723 bound protein eluted with the buffer 2 containing 300 mM Imidazole. The protein was refolded by
724 dialysis overnight against buffer 3 (20 mM Tris pH 7.0, 100 mM NaCl, 200 µM $ZnSO_4$ and 2 mM
725 DTT).
726
727 The refolded TAZ2 was incubated with His-tagged TEV protease (1:100 w/w) for 14-16 h at 4 °C.
728 Subtractive Ni-NTA chromatography was used to remove the residual His-tag and TEV protease. The
729 cleaved TAZ2 was further purified on a 5ml HiTrap SP HP cation exchange column (Cytiva)
730 preequilibrated in buffer 4 (20 mM Tris pH 7.0, 100 mM NaCl, 5 µM $ZnSO_4$ and 1 mM Dithiothreitol
731 (DTT)) and eluted using a 20 CV NaCl gradient. The peak containing TAZ2 was further purified
732 using a HiLoad 16/60 Superdex 75 column (Cytiva) preequilibrated with buffer 5 (20 mM Tris pH
733 7.0, 300 mM NaCl, 5 µM $ZnSO_4$ and 1 mM DTT). The purified protein was concentrated using a
734 prewashed Amicon Ultra-10 concentrator (molecular weight cut off 10 kDa; EMD Millipore), flash
735 frozen in liquid N2 and stored in -80°C.
736
737 Unlabeled, ^{15}N- and $^{15}N/^{13}C$-labelled NUT fragments were produced as insoluble inclusion bodies in
738 *E. coli* and purified as described above. After Ni-NTA purification, the protein was dialyzed and
739 refolded overnight at 4°C against 1L buffer 5 (20 mM Tris pH 7.0, 300 mM NaCl, 1 mM DTT and
740 10% glycerol). Refolded His-GST-NUT fusion proteins were incubated with His-tagged TEV
741 protease (1:100 w/w) for 14-16 h at 4 °C. Subtractive Ni-NTA chromatography was used to remove
742 the residual His-GST-tag and TEV protease. The cleaved NUT proteins were applied to a 5ml HiTrap
743 Q HP anion exchange column (Cytiva) in buffer 4 without $ZnSO_4$ and eluted in a 20 CV NaCl
744 gradient. The peak containing NUT was further purified by gel filtration on a Superdex 75 Increase
745 10/300 GL column (Cytiva) equilibrated in buffer 5 without $ZnSO_4$. The final proteins were

746 concentrated in a prewashed Amicon Ultra-15 Centrifugal filter (molecular weight cut off 3 kDa;
747 EMD Millipore), flash-frozen in liquid nitrogen and stored at -80 °C.
748
749 The GST-E1A amino acids 1-289 and GST-p53 AD amino acids 1-61 proteins were expressed in *E.*
750 *coli* BL21 (DE3) cells. Cell pellets were resuspended in lysis buffer resuspended and sonicated in
751 lysis buffer (20 mM Tris-HCl pH 7.5, 300 mM NaCl, 0.5 mM TCEP), supplemented with EDTA-free
752 protease inhibitors (Roche), and 10 µl of benzonase nuclease (Sigma-Aldrich) and lysed by
753 sonication. The lysate was clarified by centrifugation for 1h in a SS-34 rotor (Sorvall) at 12000 rpm
754 and applied to a Glutathione Sepharose 4 Fast Flow resin according to instructions from the
755 manufacturer (Cytiva). The resin was washed with 20 CV lysis buffer and the protein was eluted in
756 lysis buffer containing 20 mM reduced L-Glutathione. The protein solution was then dialyzed
757 overnight against lysis buffer to remove L-Glutathione and then applied to a 5 ml HiTrap Q HP anion
758 exchange column (Cytiva) and further purified by gel filtration on a Superdex 75 Increase 10/300 GL
759 column (Cytiva) as previously described for the NUT fragments.
760
761 The BRD4 GFP-BD1-BD2, GFP-BD1-BD2 N140A/N433A, GFP-BD1-BD2 N140A and GFP-BD1-
762 BD2 N433A were all expressed in *E. coli* BL21 (DE3) cells. The cells were sonicated in lysis buffer
763 (20 mM Tris-HCl pH 7.5, 300 mM NaCl, 0.5 mM TCEP) and the lysate was clarified as previously
764 described for the other proteins. The clarified lysate was applied to Ni^{2+} charged IMAC Sepharose 6
765 FF (Cytiva) beads preequilibrated with lysis buffer containing 20 mM Imidazole. The column was
766 washed with 20 column volumes (CVs) of lysis buffer and the bound proteins eluted with the lysis
767 buffer containing 300 mM Imidazole. Imidazole was removed by dialysis overnight against 1L lysis
768 buffer and the proteins were loaded on a 5 ml HiTrap SP HP cation exchange column (Cytiva) as
769 described for TAZ2 and further purified using a HiLoad 16/600 Superdex 200 column (Cytiva)
770 preequilibrated with 20 mM Tris pH 7.0, 300 mM NaCl and 1 mM DTT. The purified proteins were
771 concentrated using a prewashed Amicon Ultra-10 concentrator (molecular weight cut off 30 kDa;
772 EMD Millipore), flash frozen in liquid N2 and stored in -80°C.
773
774 The GFP-(Bromo)5 and GFP-(Bromo)5 N140A were purified as described previously (Gibson et al.,
775 2019). The co-expressed *S. cerevisiae* histones octamer was purified as described in Migl et al. (Migl
776 et al., 2020). NUT peptides were ordered from Proteogenix.
777
778 **HAT assays.** The p300 autoacetylation and substrate acetylation assays were performed using [^{14}C]
779 acetyl-CoA (Perkin-Elmer). Autoacetylation of p300 was quantified by autoradiography after SDS-
780 PAGE gel analysis. The acetylation reaction was performed for 30 minutes at 30°C in 1x HAT buffer
781 (20 mM Tris-HCl pH 7.5, 100 mM NaCl, 1 mM DTT, 10 % glycerol and 1x Complete EDTA-free
782 protease inhibitor (Roche)) with 2.5 µM p300s or p300 core and 50 µM [^{14}C] acetyl-CoA with or
783 without increasing concentrations of the different substrates (NUT fragments, NCP, E1A). 5 µl of the
784 reaction was quenched by addition of 2.5 µl of 3x SDS gel loading buffer followed by analysis on a 4-
785 20% SDS-PAGE gel. The gels were stained with Quick Coomassie Stain (Generon), fixed for 30 min
786 in enhancer solution (KODAK ENLIGHTNING Rapid Autoradiography Enhancer, Perkin Elmer) and
787 dried for 2 hours using a Bio-Rad Gel Dryer. The ^{14}C signal was quantified using phosphor imaging
788 (Typhoon, Cytiva).
789
790 ***In vitro* nucleosome acetyltransferase assays.** Nucleosome acetylation reactions were performed in
791 20 µl volume in acetylation buffer (20 mM Tris pH 7.5, 100 mM NaCl, 1 mM DTT, 10% glycerol and
792 complete Protease Inhibitor EDTA-free (Roche)) with 50 µM Acetyl-CoA, 2.5 µM of p300s or p300
793 core and 2 µM of nucleosome core particles (NCPs). Control experiments contained only NCPs and
794 Acetyl-CoA without p300. The reactions were incubated for 30 minutes at 30°C and stopped by
795 addition of 1x SDS loading buffer. Each condition was performed in duplicate. The samples were
796 then analyzed by SDS-PAGE and mass spectrometry.
797
798 **Multi angle laser light scattering-size exclusion chromatography.** SEC-MALLS was performed at
799 a flow rate of 0.5 ml/min on a Superdex 75 Increase 10/300 GL column equilibrated in buffer (20 mM

800 HEPES pH7.0, 300 mM NaCl, 5 µM $ZnSO_4$, 0.5 mM TCEP). 50 µl of TAZ2, NUT4 or the
801 TAZ2:NUT4 complex at 2 mg/ml were injected onto the column and multi angle laser light scattering
802 was recorded with a laser emitting at 690 nm using a DAWN-EOS detector (Wyatt Technology
803 Corp). The refractive index was measured using a RI2000 detector (Schambeck SFD). The molecular
804 weight was calculated from differential refractive index measurements across the center of the elution
805 peaks using the Debye model for protein using ASTRA software version 6.0.5.3.
806
807 **Biolayer interferometry assay.** BLI measurements were performed with a ForteBio Octet RED384
808 instrument and ForteBio biosensors. Data analyses was done using ForteBio Data Analysis 9.0
809 software. Kinetics assays were carried out at 25 °C using settings of Standard Kinetics Acquisition
810 rate (5.0 Hz, averaging by 20) at a sample plate shake speed of 1000 rpm. The GST-tagged NUT8
811 wild type and mutants were loaded onto Anti-GST biosensors and the TAZ2 protein was used as an
812 analyte. The GST-NUT-loaded Anti-GST biosensors were dipped in kinetic buffer (1x PBS, 0.1%
813 BSA, 0.02 % Tween 20) to establish a baseline time course and then dipped into wells containing
814 TAZ2 (1723-1836) at various concentrations diluted in the same kinetic buffer to monitor NUT-TAZ2
815 binding. The dissociation step was monitored by dipping the biosensors back into the wells used to
816 collect the baseline time course. To monitor binding due to nonspecific interactions of TAZ2 with the
817 biosensors, Anti-GST biosensors were used as controls for every analyte concentration and a double
818 referencing method was used for data subtraction and analysis. The subtracted binding curves were
819 analysed and plotted as a steady-state response to obtain the dissociation constant K_d value.
820
821 **Limited proteolysis.** To identify stable variants of NUT we performed limited proteolysis by Trypsin
822 and Chymotrypsin. 100µl of the purified CH3-NUT-F1c complex (250 µg) and TAZ2-NUT4
823 complex (250 µg) were incubated at 4 °C with Trypsin or Chymotrypsin with a ratio of 1:100 (w/w).
824 At the indicated time points (30 min, 2 hours, overnight), 30 µl of the reaction was quenched by
825 addition of 15 µl of 3x SDS gel loading buffer followed by analysis on 4-20 % SDS-PAGE gel. The
826 stable fragments on gel were analysed by acid hydrolysis and mass spectrometry at the Proteomics
827 Core Facility (EMBL, Heidelberg).
828
829 **SAXS analysis.** X-ray scattering data were collected on the NUT-F1c sample at 100 µM in phase
830 separation buffer: 20 mM Tris pH 7.2 mM DTT, 125 mM NaCl and 10% (w/v) PEG 6000 at the B21
831 BioSAXS beamline of the Diamond Light Source (Chilton, Oxfordshire, UK). The data were analysed
832 with the ATSAS package (Franke et al., 2017). Data collected from the sample were substracted from
833 buffer scattering. R_g values were obtained from the Guinier approximation $sR_g < 1.3$ using Primus
834 (Petoukhov et al., 2012). Distance distribution functions p(r) were computed from the entire scattering
835 curve using GNOM (Petoukhov et al., 2012).
836
837 ***In vitro* NUT phase separation assay.** Phase separation of purified GST-NUT-F1c *in vitro* was done
838 phase separation buffer. The concentrations of GST-NUT-F1c used were 0-200 µM. A GST control
839 was used in the same concentration range under identical conditions. The droplets were visually
840 observed and turbidity of the sample (OD_{600}) quantified using NanoDrop (Thermo scientific).
841
842 **GST pulldowns.** For GST pulldowns, 50 µg of GST-tagged NUT constructs were mixed at an
843 equimolar concentration with binding partners in 50 µl pulldown buffer (20 mM HEPES pH 8.0, 300
844 mM NaCl, 0.5 mM TCEP, 5µM $ZnSO_4$, 0.1% Triton X-100) containing 25 µl of a 50 % slurry of
845 GST Sepharose 4 Fast Flow beads (Cytiva) per reaction. Reactions were incubated for 30 min at 4 °C.
846 Twenty-five microliters of the reaction were withdrawn as the reaction input and the remainder was
847 washed 5 times with 500 µl of pulldown buffer. Samples were boiled in 1x sample loading buffer for
848 5 min and analysed by SDS-PAGE.
849
850 **Luciferase reporter assays.** Cos7 cells were co-transfected for 36 hours with β-Galactosidase
851 reporter plasmid and UAS-promoter luciferase reporter plasmid either alone or with GAL4 DNA
852 binding domain (DBD) plasmid or increasing amount of GAL4-DBD-NUT-F1c plasmid. Cells were
853 then washed and incubated 15 min at RT with Luciferase lysis buffer (1% Triton X-100, 10%

854 Glycerol, 2 mM EDTA, 25 mM Tris-HCl pH 7.8). Luciferase activity was measured directly after
855 mixing 10µl of cellular extract with 50 µl of Luciferase substrate (Luciferase assay kit, Stratagene).
856 Normalization was made by measuring the β-Gal activity after 1-hour incubation of 7.5 µl of cellular
857 extract with 50 µl of β-Gal substrate (β-Gal detection kit II, Clontech).
858
859 **Proteomics of histone modifications.** For the identification and quantification of histone acetylation
860 following *in vitro* HAT assays, we followed the previously published procedure (Goudarzi et al.,
861 2016; Shiota et al., 2018). In brief, reconstituted NCPs were incubated with 100µM acetyl-CoA, as
862 well as purified p300s (340-2,094) or the p300 core domain (1,043-1,666) for 30 min at 30°C. HPLC-
863 MS/MS was used to quantify site specific H2A, H2B, H3 and H4 acetylation by label-free
864 quantification. The peak area of each histone peptide was then normalized. Two technical replicate
865 experiments were done.
866
867 **Isolation and Purification of 1x601 Widom DNA.** Carrier plasmids of 1x Widom 601 repeats were
868 purified using QIAGEN Plasmid Giga kit from 6L LB culture according to the manufacturer's
869 instructions. 1x arrays DNA were cut from carrier plasmid DNA by incubation overnight with 5,000
870 units of *EcoR*V-HF restriction endonuclease (New England Biolabs) in 1x CutSmart Buffer (20 mM
871 Tris,OAc, pH 7.9, 50 mM KOAc, 10 mM $Mg[OAc]_2$, 0.1 mg/mL BSA). The excised DNA fragments
872 were separated from the linearized plasmid by PEG precipitation. 0.192 volume of NaCl and 8% PEG
873 6000 were added to the DNA sample and incubated for 1h on ice, the sample was then centrifuged for
874 20 min at 4 °C, 27000 g. the *EcoR*V fragments contained in the supernatant were precipitated by the
875 addition of 2.5 volumes of 100% cold ethanol. The DNA fragments were air dried for 10 min and
876 dissolved in buffer TE (10 mM Tris/HCl, pH 8.0, 1 mM EDTA). Purity of the extracted 12x601 and
877 1x601 fragments were verified on 0.7% agarose gels and the concentration measured by 260 nm
878 absorbance on a NanoDrop spectrophotometer (Thermo Scientific).
879
880 **Isolation and Purification of 12x Widom 601 Array DNA.** 12x601 DNA template was prepared
881 as described previously (Dorigo et al., 2003). In short, 12-mer DNA with177 bp repeats of
882 the 601 sequence separated from the rest of the plasmid by *Eco*RV sites were expressed in
883 *E.coli* strain DH5a. The DNA was then extracted by alkaline lysis and purified on a
884 Sepharose-6 column. The DNA template was separated from the plasmid by *EcoR*V-HF
885 digestion and PEG6000 precipitation.
886
887 **Histones octamer preparation.** Wild type human histones (H2A, H2B, H3 and H4) and the cysteine
888 mutant Xenopus H4 S47C were individually expressed in *E. coli* strain Rosetta 2 DE3 pLysS and
889 purified following the protocol described (Luger et al., 1999), but using a RESOURCE S 6 ml cation
890 exchange chromatography column. For octamer reconstitution, equimolar ratios of the four histones
891 were refolded together in the presence of 5 mM β-mercaptoethanol. The octamer was then separated
892 from dimers by gel filtration using a Superdex 200 column (Cytiva). Two batches of octamers have
893 been generated: one fully wild-type human octamer (unlabelled octamer) and an octamer formed by
894 wild-type human H2A, H2B, H3 and Alexa Fluor™ 594 C5 Maleimide labelled *Xenopus* H4 S47C
895 (labelled octamer).
896
897 **Fluorescent labelling of histones.** The *Xenopus* H4 S47C mutant histone was labelled using Alexa
898 Fluor™ 594 C5 Maleimide following the protocol from (Gibson et al., 2019). In short, lyophilised H4
899 S47C was resuspended in 7M urea, 500mM Tris-HCl pH 8 and incubated with Tris-neutralized TCEP
900 to a final concentration of 2 mM for 1 hr and 30 min at RT. Alexa Fluor™ 594 C5 Maleimide stock
901 solution was added dropwise to a 1.5 molar excess and the mix was incubated for 4 hr at RT in the dark.
902 The reaction was quenched by the addition of β-mercaptoethanol. The histone was then purified from
903 the free dye by ion exchange chromatography using a HiTrap SP HP cation exchange column followed
904 by dialysis into ultra-pure water with 5 mM β-mercaptoethanol.
905
906 **Mononucleosome assembly.** DNA and *Saccharomyces cerevisiae* histones octamer were mixed in a
907 1:0.5 molar ratio. Nucleosomes were reconstituted by salt gradient dialysis method and dialysed

908 against buffer 20 mM Tris-HCl, pH 8.0, 1 mM EDTA, 1 mM DTT with continuous decrease of NaCl
909 concentrations (1.5, 1, 0.6 and 0.25 M) at 4 °C, 3h each dialysis step with the third dialysis step
910 proceeding overnight using mini dialysis units (10,000 Da MWCO, Pierce Slide-a-lyzer). The
911 reconstituted nucleosomes were quality controlled by electrophoretic mobility shift assays on 5%
912 acrylamide native gels with 0.25x TBE running buffer.
913
914 **12x Nucleosome array assembly, acetylation and phase separation.** Chromatin was reconstituted
915 *in vitro* by assembling the 12-mer DNA with histone octamers by step-wise salt dialysis as described
916 previously (Dorigo et al., 2003), but using KCl instead of NaCl. The optimal octamer to DNA ratio
917 was determined empirically. A mix of labelled and unlabelled histone octamer was used. The ratio of
918 labelled to unlabelled histone octamer was also determined empirically. The reconstituted 12-mer
919 nucleosome arrays were quality controlled by *Sca*I restriction enzyme digestion to isolate single
920 nucleosome particles and by electrophoretic mobility shift assays on 1% agarose gel in 0.5x TAE
921 12x601 nucleosome arrays at 2 μM mono-nucleosome concentration were incubated with 1 μM of the
922 p300 core domain in Acetylation buffer (20 mM Tris-HCl pH 7.0, 100 mM NaCl, 10% glycerol, 1
923 mM DTT) for 30 min at 30 °C. The non-acetylated chromatin reactions were incubated under
924 identical conditions but without p300 core enzyme. After acetylation, 5 μM BRD4 GFP-Bromo$_5$,
925 GFP-Bromo$_5$ N140A, 10 μM GFP-BD1-BD2, 10 μM GFP-BD1-BD2 N140A, 10 μM GFP-BD1-BD2
926 N433A or 10 μM GFP-BD1-BD2 N140A/N433A were added to nucleosomal arrays for a final
927 concentration of 1 μM mono-nucleosome in phase separation buffer (25 mM Tris, pH7.5, 150 mM
928 KOAc, 1 mM MgOAc, 5% glycerol, 5 mM DTT, 0.1 mM EDTA, 0.1 mg/mL BSA) (Gibson et al.,
929 2019).
930
931 **Microscopy of chromatin droplets.** For confocal microscopy image acquisition, a Zeiss LSM 980
932 Airyscan 2 microscope equipped with a Plan-Apochromat 63x/1.40 Oil DIC f/ELYRA and ZEN Blue
933 3 acquisition and analysis software was used. Samples were imaged in 384 well glass bottom plates
934 for microscopy which were prepared as described in (Gibson et al., 2019). In short, microscopy plates
935 were washed with 5% Hellmanex, etched with 1 M NaOH and treated with 25 mg/mL 5K mPEG-
936 silane. Prior to use, individual wells were passivated by incubation with freshly prepared 100 mg/mL
937 BSA.
938
939 **Cross-linking mass spectrometry.** Purified solutions of both NCPs and p300 core-CH3 (1043-1817)
940 were diluted to a concentration between 0.5 and 1 mg/ml in 20 mM HEPES pH 7.0, 300 mM NaCl, 1
941 mM DTT and 5 μM $ZnCl_2$ and cross linked using a homobifunctional, isotopically-coded crosslinker
942 DiSuccinimidyl Suberate DSS-H12/D12 (Creative Molecules Inc.) at a concentration of 2 mM for 30
943 min at 35°C 600 rpm. The cross-linking reaction was then quenched with 0.1 volumes of 1M
944 Ammonium bicarbonate for 10 min at 35 °C 600 rpm. The sample was then treated with 0.8 volumes
945 of 10 M urea and 250 mM Ammonium bicarbonate as well as 0.05 volumes RapiGest SF Surfactant
946 (Waters, cat. No. 186008090) and sonicated for 1 min in an ultrasound bath. DTT was later added
947 with a final concentration of 10 mM, incubated for 30 min at 37 °C and freshly prepared
948 Iodoacetamide was added to a final concentration of 15 mM and incubated for 30 min at room
949 temperature in the dark. The protein was sequentially digested with Endoproteinase Lys-C and
950 Trypsin. The enzymes were added at an enzyme to substrate ratio of 1:100 for LysC and 1:50 for
951 Trypsin and the reaction incubated for 3-4 h at 37°C. The reaction was started by LysC followed by
952 Trypsin addition after 4h. After digestion, the sample was acidified with Trifluoroacetic acid (1% v/v
953 final concentration) at 37°C for 30 min, spun down at 17,000 g for 5 min and the peptides were
954 fractionated by peptide size-exclusion chromatography. The mass spectrometry experiment and cross-
955 links identification were performed by the EMBL Proteomics core facility.
956
957 **Immunofluorescence and drug treatment.** Cos7 cells were seeded in glass coverslips (Lab-Tek),
958 and GFP and RFP bearing constructs were transfected by Lipofectamine 2000. Twenty-four hours
959 later, cells were washed with PBS and fixed with 4% paraformaldehyde for 15 min, followed by
960 permeabilization with 0.2% Triton-X100 and 1 × PBS for 10 min at room temperature. After being
961 blocked with 5% dry milk, 0.2% Tween 20, and 1 × PBS at RT for 30 min, slides were incubated with

anti-acH4 antibody (1:100 dilution, Millipore) or anti-HDAC1 antibody (1:100 dilution, Cell Signaling Technology) in 1% dry milk, 0.1% Tween 20, and 1 × PBS in a humidified chamber at 4°C overnight and then washed three times for 5 min each in the antibody dilution buffer. The secondary antibodies were diluted at 1:500 in the same buffer and incubated in a humidified chamber for 30 min at 37°C, and then washed as for the primary antibodies. The DNA was counterstained by DAPI, and the slides were mounted in Dako fluorescent mounting medium. For the drug treatment assays, twenty-four hours after being transfected with GFP and RFP bearing constructs, Cos7 cells were treated with DMSO (Sigma), 1,6-hexanediol (10%, 1 hour, Sigma), A485 (3 μM, 1 hour, Selleck), JQ1 (1 μM, 1 hour, Selleck), TSA (0.3 μM, 12 hours, Selleck) or CBP30 (1 μM, 1 hour, Selleck), then the cells were washed with PBS and fixed with 4% paraformaldehyde for 15 min.

Co-immunoprecipitation. Cell pellets were lysed in 300 mM NaCl buffer (20 mM HEPES-KOH pH 7.9, 300 mM NaCl, 3 mM $MgCl_2$, 0.1% NP-40, 1X protease inhibitor cocktail (Roche), 1X phosphatase inhibitor cocktail-1 (Sigma) and 10 mM sodium butyrate) for 30 min at 4 °C with rotation. After a 15 min centrifugation at 12,000g at 4°C, the supernatants were collected and separated into input and immunoprecipitate (IP) lysates. IP lysates were mixed with GFP-selector (pre-washed with 300 mM NaCl buffer three times, NanoTag) and rotated overnight at 4 °C. After washing with 300 mM NaCl buffer, IPs were released by adding Laemmli sample buffer to beads and boiling for 5 min at 100°C.

Fluorescence recovery after photobleaching (FRAP). Live imaging and fluorescence recovery after photobleaching experiments (FRAP) were performed with the LSM710 Confocor3 confocal microscope (Carl Zeiss), equipped with the Plan-Apochromat C 63X /1.4 oil-immersion objective. FRAP area, time and time interval (1 image every 783ms) were maintained identical between the different BRD4-NUT mutants and repeat measurements (N=3-4, 45 to 65 foci measured per conditions) in order to photobleach 3-6 foci at the same time. To compare recovery kinetics against BRD4-NUT wild-type, FRAP measurements were fitted to a single exponential curve, $I_{(t)}=I_{(0)} + k_1e^{-k2t}$ (performed with ZEN software; Carl Zeiss Microscopy) to determine the characteristic time of recovery. Values of τ (1/ k2) were compiled and statistical significance was tested using the Student's t-test (Excel).

NMR experiments. Backbone resonances of both proteins free in solution were assigned by measuring HNCO, HNCA, and HN(CO)CA spectra on ^{15}N,^{13}C-labelled samples at 600 (NUT7) and 700 (TAZ2) MHz. We were able to assign 87% (95%) of the NH pairs, 72% (82%) of the CO resonances and 88% (96%) of the CA resonances in the backbone of NUT7 (TAZ2).

Side-chain resonances of both proteins free in solution were assigned by measuring HBHA(CO)NH, H(CCO)NH, and CC(CO)NH spectra on ^{15}N,^{13}C-labelled samples at 600 (NUT7) and 700 (TAZ2) MHz. We were able to assign 70% (55%) of the HA resonances, 57% (45%) of the HB resonances, and 45% (53%) of the CB resonances in NUT7 (TAZ2), as well as part of the γ-protons.

To determine the binding site of NUT7 on TAZ2, we measured ^{1}H-^{15}N HSQC spectra on ^{15}N-labelled TAZ2 before and after adding unlabelled NUT7. For each of the assigned peaks in the spectra we calculate the chemical shift perturbations (CSP) defined as

$$CSP = \sqrt{\frac{1}{2}\left(\Delta\delta_H^2 + (0.14 \cdot \Delta\delta_N)^2\right)},$$

in which $\Delta\delta_H$ and $\Delta\delta_N$ are the chemical shift differences upon adding NUT7 in the ^{1}H and ^{15}N dimensions, respectively. We used the procedure described by Schumann et al. (Schumann et al., 2007) to determine whether measured CSPs are significant or not. We used the same approach to map the binding site on NUT7 monitoring a titration of a solution of ^{15}N-labelled NUT7 with unlabelled TAZ2 using ^{1}H-^{15}N HSQC spectra.

Both ^{13}C- and ^{15}N-HSQC-NOESY spectra on a sample of ^{15}N,^{13}C-labelled TAZ2 to which one equivalent of unlabelled NUT7 was added and ^{15}N-HSQC-NOESY spectra on ^{15}N-labelled NUT7 in

admixture with one equivalent of unlabelled TAZ2 were measured using standard pulse sequences. All NOESY spectra were measured at 950 MHz with a mixing time of 100 ms.

HADDOCK docking. We used the HADDOCK protocol (Dominguez et al., 2003) with experimental information from titrations and NOESY spectra to derive a structural model of the interaction. We used the NMRbox platform (Maciejewski et al., 2017) to carry out the calculations. In a first step, we used the results of the titration experiments to derive ambiguous distance restraints (AIRs) describing the binding interface, and we used these AIRs as input for HADDOCK to dock extended conformations of NUT7 on the TAZ2 structure derived from PDB 2mzd. The best 200 structures resulting from the calculations were clustered based on the fraction of common contacts (FCC). The resulting clusters were sorted according to their agreement with the AIRs. Structures in the best cluster display the interaction of residues P448-E454 in NUT7 with TAZ2. Thus, we used the Flexible-Meccano algorithm (Ozenne et al., 2012) to generate an ensemble of 100 conformers of NUT7, in which the conformation of residues P448-E454 is the same as in the structure resulted from the HADDOCK calculation, whereas the rest of the chain behaves like a statistical coil. Then, we used HADDOCK again to dock this ensemble of structures on the same TAZ2 conformation as above. In this run, in addition to the same AIRs as in the preliminary run, we used distance restraints derived from NOESY spectra between S1726 in TAZ2 and residues L463 and A464 in NUT7. We also used TALOS-N (Shen and Bax, 2013) to derive restraints on the backbone dihedral angles of residues P448-E454 from chemical shift values. We repeated this calculation ten times with different initial seeds and velocities. Finally, the best 200 structures from each of the ten runs were clustered based on the FCC. The resulting clusters were sorted according to their agreement with the AIRs and NOE-based restraints. Then, from the best-ranked cluster in each of the runs, we selected the structure with the best HADDOCK score (which is a linear combination of various energy terms and buried surface area), thereby obtaining a final set of 10 structures.

Cryo-electron microscopy grid preparation, data collection and image processing

Quantifoil R1.2/1.3 Au 300 grids were glow discharged for 5 min at 40 mA on a Quorum Gloqube glow-discharge unit prior to application of the sample. 3 µl of 1 µM final concentration of the mononucleosome particles in buffer 20 mM Tris-HCl, pH8.0, 250 mM NaCl, 1 mM EDTA, 1 mM DTT were applied to the grid, blotted for 3 s at blot force 10 and plunge frozen into liquid ethane using a Vitrobot Mark IV (FEI Thermo Fisher), which was set at 4°C and 100% humidity. Cryo-EM data was collected on a Thermo Fisher Scientific Titan Krios G3 transmission electron microscope at the LISCB at the University of Leicester. Electron micrographs were recorded using a K3 direct electron detector (Gatan Inc.) at a dose rate of 15 e^-/pix/sec and a calibrated pixel size 1.086 Å. Focusing was performed over a range between -2.3 and -1.1 µm in 0.3 µm intervals. Image processing of the NCPs was performed as follows: movie stacks were corrected for beam-induced motion and then integrated using MotionCor2 (Zheng et al., 2017). All frames were retained and a patch alignment of 4 x 4 was used. Contrast transfer function (CTF) parameters for each micrograph were estimated by Gctf (Zhang, 2016). Integrated movies were inspected with Relion-3.1 for further image processing (243 movies). Initial particle sets were picked manually, extracted, and subjected to 2D classification in Relion 3.1 (Zivanov et al., 2018). Resulting classes corresponding to protein complexes were subsequently employed as references for auto-picking in Relion 3.1. Particle extraction was carried out from micrographs using a box size of 128 pixels (pixel size: 1.08 Å/pixel). An initial dataset of 80764 particles was cleaned by several iterations of 2D classification, classes exhibiting clear secondary structure features were selected for 3D classification. After iterative rounds of 3D classifications, well defined classes were selected and global refinement was performed.

1060 **References**

1061 1 Ahmad, K., and Henikoff, S. (2001). Modulation of a transcription factor counteracts
1062 heterochromatic gene silencing in Drosophila. Cell *104*, 839-847.
1063 2 Ahn, J.H., Davis, E.S., Daugird, T.A., Zhao, S., Quiroga, I.Y., Uryu, H., Li, J., Storey, A.J.,
1064 Tsai, Y.H., Keeley, D.P.*, et al.* (2021). Phase separation drives aberrant chromatin looping and cancer
1065 development. Nature *595*, 591-595.
1066 3 Alekseyenko, A.A., Walsh, E.M., Wang, X., Grayson, A.R., Hsi, P.T., Kharchenko, P.V.,
1067 Kuroda, M.I., and French, C.A. (2015). The oncogenic BRD4-NUT chromatin regulator drives
1068 aberrant transcription within large topological domains. Genes Dev *29*, 1507-1523.
1069 4 Alekseyenko, A.A., Walsh, E.M., Zee, B.M., Pakozdi, T., Hsi, P., Lemieux, M.E., Dal Cin,
1070 P., Ince, T.A., Kharchenko, P.V., Kuroda, M.I.*, et al.* (2017). Ectopic protein interactions within
1071 BRD4-chromatin complexes drive oncogenic megadomain formation in NUT midline carcinoma.
1072 Proc Natl Acad Sci U S A *114*, E4184-E4192.
1073 5 Allen, B.L., and Taatjes, D.J. (2015). The Mediator complex: a central integrator of
1074 transcription. Nat Rev Mol Cell Biol *16*, 155-166.
1075 6 Aparicio, O.M., and Gottschling, D.E. (1994). Overcoming telomeric silencing: a trans-
1076 activator competes to establish gene expression in a cell cycle-dependent way. Genes Dev *8*, 1133-
1077 1146.
1078 7 Apostolou, E., and Thanos, D. (2008). Virus Infection Induces NF-kappaB-dependent
1079 interchromosomal associations mediating monoallelic IFN-beta gene expression. Cell *134*, 85-96.
1080 8 Attar, N., and Kurdistani, S.K. (2017). Exploitation of EP300 and CREBBP Lysine
1081 Acetyltransferases by Cancer. Cold Spring Harb Perspect Med *7*.
1082 9 Avantaggiati, M.L., Carbone, M., Graessmann, A., Nakatani, Y., Howard, B., and Levine,
1083 A.S. (1996). The SV40 large T antigen and adenovirus E1a oncoproteins interact with distinct
1084 isoforms of the transcriptional co-activator, p300. EMBO Journal *15*, 2236-2248.
1085 10 Basu, S., Mackowiak, S.D., Niskanen, H., Knezevic, D., Asimi, V., Grosswendt, S.,
1086 Geertsema, H., Ali, S., Jerkovic, I., Ewers, H.*, et al.* (2020). Unblending of Transcriptional
1087 Condensates in Human Repeat Expansion Disease. Cell *181*, 1062-1079 e1030.
1088 11 Black, J.C., Mosley, A., Kitada, T., Washburn, M., and Carey, M. (2008). The SIRT2
1089 deacetylase regulates autoacetylation of p300. Mol Cell *32*, 449-455.
1090 12 Boija, A., Klein, I.A., Sabari, B.R., Dall'Agnese, A., Coffey, E.L., Zamudio, A.V., Li, C.H.,
1091 Shrinivas, K., Manteiga, J.C., Hannett, N.M.*, et al.* (2018). Transcription Factors Activate Genes
1092 through the Phase-Separation Capacity of Their Activation Domains. Cell *175*, 1842-1855 e1816.
1093 13 Boija, A., Klein, I.A., and Young, R.A. (2021). Biomolecular Condensates and Cancer.
1094 Cancer Cell *39*, 174-192.
1095 14 Cabianca, D.S., Munoz-Jimenez, C., Kalck, V., Gaidatzis, D., Padeken, J., Seeber, A.,
1096 Askjaer, P., and Gasser, S.M. (2019). Active chromatin marks drive spatial sequestration of
1097 heterochromatin in C. elegans nuclei. Nature *569*, 734-739.
1098 15 Carey, M., Lin, Y.S., Green, M.R., and Ptashne, M. (1990). A mechanism for synergistic
1099 activation of a mammalian gene by GAL4 derivatives. Nature *345*, 361-364.
1100 16 Carpenter, A.E., Memedula, S., Plutz, M.J., and Belmont, A.S. (2005). Common effects of
1101 acidic activators on large-scale chromatin structure and transcription. Mol Cell Biol *25*, 958-968.
1102 17 Chambeyron, S., and Bickmore, W.A. (2004). Chromatin decondensation and nuclear
1103 reorganization of the HoxB locus upon induction of transcription. Gene Dev *18*, 1119-1130.
1104 18 Chan, H.M., and La Thangue, N.B. (2001). p300/CBP proteins: HATs for transcriptional
1105 bridges and scaffolds. J Cell Sci *114*, 2363-2373.
1106 19 Cho, W.K., Spille, J.H., Hecht, M., Lee, C., Li, C., Grube, V., and Cisse, II (2018). Mediator
1107 and RNA polymerase II clusters associate in transcription-dependent condensates. Science *361*, 412-
1108 415.
1109 20 Chong, S., Dugast-Darzacq, C., Liu, Z., Dong, P., Dailey, G.M., Cattoglio, C., Heckert, A.,
1110 Banala, S., Lavis, L., Darzacq, X.*, et al.* (2018). Imaging dynamic and selective low-complexity
1111 domain interactions that control gene transcription. Science *361*.
1112 21 Creyghton, M.P., Cheng, A.W., Welstead, G.G., Kooistra, T., Carey, B.W., Steine, E.J.,
1113 Hanna, J., Lodato, M.A., Frampton, G.M., Sharp, P.A.*, et al.* (2010). Histone H3K27ac separates

active from poised enhancers and predicts developmental state. Proc Natl Acad Sci U S A *107*, 21931-21936.
22 Dames, S.A., Martinez-Yamout, M., De Guzman, R.N., Dyson, H.J., and Wright, P.E. (2002). Structural basis for Hif-1 alpha /CBP recognition in the cellular hypoxic response. Proc Natl Acad Sci U S A *99*, 5271-5276.
23 Dancy, B.M., and Cole, P.A. (2015). Protein lysine acetylation by p300/CBP. Chem Rev *115*, 2419-2452.
24 De Bosscher, K., Vanden Berghe, W., and Haegeman, G. (2003). The interplay between the glucocorticoid receptor and nuclear factor-kappaB or activator protein-1: molecular mechanisms for gene repression. Endocr Rev *24*, 488-522.
25 Delvecchio, M., Gaucher, J., Aguilar-Guerreri, C., Ortega, E., and Panne, D. (2013). Structure of the p300 catalytic core and implications for chromatin targeting and HAT regulation. Nature Structural and Molecular Biology *21*.
26 Devaiah, B.N., Case-Borden, C., Gegonne, A., Hsu, C.H., Chen, Q., Meerzaman, D., Dey, A., Ozato, K., and Singer, D.S. (2016). BRD4 is a histone acetyltransferase that evicts nucleosomes from chromatin. Nat Struct Mol Biol *23*, 540-548.
27 Dhalluin, C., Carlson, J.E., Zeng, L., He, C., Aggarwal, A.K., and Zhou, M.M. (1999). Structure and ligand of a histone acetyltransferase bromodomain. Nature *399*, 491-496.
28 Dixon, J.R., Selvaraj, S., Yue, F., Kim, A., Li, Y., Shen, Y., Hu, M., Liu, J.S., and Ren, B. (2012). Topological domains in mammalian genomes identified by analysis of chromatin interactions. Nature *485*, 376-380.
29 Dominguez, C., Boelens, R., and Bonvin, A.M. (2003). HADDOCK: a protein-protein docking approach based on biochemical or biophysical information. Journal of the American Chemical Society *125*, 1731-1737.
30 Dorigo, B., Schalch, T., Bystricky, K., and Richmond, T.J. (2003). Chromatin fiber folding: requirement for the histone H4 N-terminal tail. J Mol Biol *327*, 85-96.
31 Dyson, H.J., and Wright, P.E. (2016). Role of Intrinsic Protein Disorder in the Function and Interactions of the Transcriptional Coactivators CREB-binding Protein (CBP) and p300. J Biol Chem *291*, 6714-6722.
32 Eagen, K.P., and French, C.A. (2021). Supercharging BRD4 with NUT in carcinoma. Oncogene *40*, 1396-1408.
33 Eberharter, A., and Becker, P.B. (2002). Histone acetylation: a switch between repressive and permissive chromatin. Second in review series on chromatin dynamics. EMBO Rep *3*, 224-229.
34 Erdel, F., Rademacher, A., Vlijm, R., Tunnermann, J., Frank, L., Weinmann, R., Schweigert, E., Yserentant, K., Hummert, J., Bauer, C.*, et al.* (2020). Mouse Heterochromatin Adopts Digital Compaction States without Showing Hallmarks of HP1-Driven Liquid-Liquid Phase Separation. Mol Cell *78*, 236-249 e237.
35 Erdel, F., and Rippe, K. (2018). Formation of Chromatin Subcompartments by Phase Separation. Biophys J *114*, 2262-2270.
36 Falk, M., Feodorova, Y., Naumova, N., Imakaev, M., Lajoie, B.R., Leonhardt, H., Joffe, B., Dekker, J., Fudenberg, G., Solovei, I.*, et al.* (2019). Heterochromatin drives compartmentalization of inverted and conventional nuclei. Nature *570*, 395-399.
37 Feng, H., Jenkins, L.M., Durell, S.R., Hayashi, R., Mazur, S.J., Cherry, S., Tropea, J.E., Miller, M., Wlodawer, A., Appella, E.*, et al.* (2009). Structural basis for p300 Taz2-p53 TAD1 binding and modulation by phosphorylation. Structure *17*, 202-210.
38 Ferrari, R., Gou, D., Jawdekar, G., Johnson, S.A., Nava, M., Su, T., Yousef, A.F., Zemke, N.R., Pellegrini, M., Kurdistani, S.K.*, et al.* (2014). Adenovirus small E1A employs the lysine acetylases p300/CBP and tumor suppressor Rb to repress select host genes and promote productive virus infection. Cell Host Microbe *16*, 663-676.
39 Ferrari, R., Pellegrini, M., Horwitz, G.A., Xie, W., Berk, A.J., and Kurdistani, S.K. (2008). Epigenetic reprogramming by adenovirus e1a. Science *321*, 1086-1088.
40 Ferreon, J.C., Martinez-Yamout, M.A., Dyson, H.J., and Wright, P.E. (2009). Structural basis for subversion of cellular control mechanisms by the adenoviral E1A oncoprotein. Proceedings of the National Academy of Sciences of the United States of America *106*, 13260-13265.

41 Filippakopoulos, P., and Knapp, S. (2012). The bromodomain interaction module. FEBS Lett *586*, 2692-2704.
42 Fisher, W.W., Li, J.J., Hammonds, A.S., Brown, J.B., Pfeiffer, B.D., Weiszmann, R., MacArthur, S., Thomas, S., Stamatoyannopoulos, J.A., Eisen, M.B.*, et al.* (2012). DNA regions bound at low occupancy by transcription factors do not drive patterned reporter gene expression in Drosophila. Proc Natl Acad Sci U S A *109*, 21330-21335.
43 Franke, D., Petoukhov, M.V., Konarev, P.V., Panjkovich, A., Tuukkanen, A., Mertens, H.D.T., Kikhney, A.G., Hajizadeh, N.R., Franklin, J.M., Jeffries, C.M.*, et al.* (2017). ATSAS 2.8: a comprehensive data analysis suite for small-angle scattering from macromolecular solutions. J Appl Crystallogr *50*, 1212-1225.
44 Fukaya, T., Lim, B., and Levine, M. (2016). Enhancer Control of Transcriptional Bursting. Cell *166*, 358-368.
45 Gaucher, J., Boussouar, F., Montellier, E., Curtet, S., Buchou, T., Bertrand, S., Hery, P., Jounier, S., Depaux, A., Vitte, A.L.*, et al.* (2012). Bromodomain-dependent stage-specific male genome programming by Brdt. EMBO J *31*, 3809-3820.
46 Ghandi, M., Huang, F.W., Jane-Valbuena, J., Kryukov, G.V., Lo, C.C., McDonald, E.R., 3rd, Barretina, J., Gelfand, E.T., Bielski, C.M., Li, H.*, et al.* (2019). Next-generation characterization of the Cancer Cell Line Encyclopedia. Nature *569*, 503-508.
47 Gibson, B.A., Doolittle, L.K., Schneider, M.W.G., Jensen, L.E., Gamarra, N., Henry, L., Gerlich, D.W., Redding, S., and Rosen, M.K. (2019). Organization of Chromatin by Intrinsic and Regulated Phase Separation. Cell *179*, 470-484 e421.
48 Gill, G., and Ptashne, M. (1988). Negative effect of the transcriptional activator GAL4. Nature *334*, 721-724.
49 Gillespie, M.A., Palii, C.G., Sanchez-Taltavull, D., Shannon, P., Longabaugh, W.J.R., Downes, D.J., Sivaraman, K., Espinoza, H.M., Hughes, J.R., Price, N.D.*, et al.* (2020). Absolute Quantification of Transcription Factors Reveals Principles of Gene Regulation in Erythropoiesis. Mol Cell *78*, 960-974 e911.
50 Goodman, R.H., and Smolik, S. (2000). CBP/p300 in cell growth, transformation, and development. Genes Dev *14*, 1553-1577.
51 Goudarzi, A., Zhang, D., Huang, H., Barral, S., Kwon, O.K., Qi, S., Tang, Z., Buchou, T., Vitte, A.L., He, T.*, et al.* (2016). Dynamic Competing Histone H4 K5K8 Acetylation and Butyrylation Are Hallmarks of Highly Active Gene Promoters. Mol Cell *62*, 169-180.
52 Green, M.R. (2005). Eukaryotic transcription activation: right on target. Mol Cell *18*, 399-402.
53 Gryder, B.E., Pomella, S., Sayers, C., Wu, X.S., Song, Y., Chiarella, A.M., Bagchi, S., Chou, H.C., Sinniah, R.S., Walton, A.*, et al.* (2019a). Histone hyperacetylation disrupts core gene regulatory architecture in rhabdomyosarcoma. Nat Genet *51*, 1714-1722.
54 Gryder, B.E., Wu, L., Woldemichael, G.M., Pomella, S., Quinn, T.R., Park, P.M.C., Cleveland, A., Stanton, B.Z., Song, Y., Rota, R.*, et al.* (2019b). Chemical genomics reveals histone deacetylases are required for core regulatory transcription. Nat Commun *10*, 3004.
55 Guertin, M.J., Zhang, X., Coonrod, S.A., and Hager, G.L. (2014). Transient estrogen receptor binding and p300 redistribution support a squelching mechanism for estradiol-repressed genes. Mol Endocrinol *28*, 1522-1533.
56 Guo, Y.E., Manteiga, J.C., Henninger, J.E., Sabari, B.R., Dall'Agnese, A., Hannett, N.M., Spille, J.H., Afeyan, L.K., Zamudio, A.V., Shrinivas, K.*, et al.* (2019). Pol II phosphorylation regulates a switch between transcriptional and splicing condensates. Nature *572*, 543-+.
57 Gurdon, J.B., Javed, K., Vodnala, M., and Garrett, N. (2020). Long-term association of a transcription factor with its chromatin binding site can stabilize gene expression and cell fate commitment. Proc Natl Acad Sci U S A *117*, 15075-15084.
58 Halford, S.E. (2009). An end to 40 years of mistakes in DNA-protein association kinetics? Biochem Soc Trans *37*, 343-348.
59 Hammitzsch, A., Tallant, C., Fedorov, O., O'Mahony, A., Brennan, P.E., Hay, D.A., Martinez, F.O., Al-Mossawi, M.H., de Wit, J., Vecellio, M.*, et al.* (2015). CBP30, a selective CBP/p300 bromodomain inhibitor, suppresses human Th17 responses. Proc Natl Acad Sci U S A *112*, 10768-10773.

1223 60 Han, X., Yu, D., Gu, R., Jia, Y., Wang, Q., Jaganathan, A., Yang, X., Yu, M., Babault, N.,
1224 Zhao, C., *et al.* (2020). Roles of the BRD4 short isoform in phase separation and active gene
1225 transcription. Nat Struct Mol Biol *27*, 333-341.
1226 61 Hansson, M.L., Popko-Scibor, A.E., Saint Just Ribeiro, M., Dancy, B.M., Lindberg, M.J.,
1227 Cole, P.A., and Wallberg, A.E. (2009). The transcriptional coactivator MAML1 regulates p300
1228 autoacetylation and HAT activity. Nucleic Acids Res *37*, 2996-3006.
1229 62 He, J., Ye, J., Cai, Y., Riquelme, C., Liu, J.O., Liu, X., Han, A., and Chen, L. (2011).
1230 Structure of p300 bound to MEF2 on DNA reveals a mechanism of enhanceosome assembly. Nucleic
1231 Acids Res *39*, 4464-4474.
1232 63 Hnisz, D., Shrinivas, K., Young, R.A., Chakraborty, A.K., and Sharp, P.A. (2017). A Phase
1233 Separation Model for Transcriptional Control. Cell *169*, 13-23.
1234 64 Ho, J.W., Jung, Y.L., Liu, T., Alver, B.H., Lee, S., Ikegami, K., Sohn, K.A., Minoda, A.,
1235 Tolstorukov, M.Y., Appert, A., *et al.* (2014). Comparative analysis of metazoan chromatin
1236 organization. Nature *512*, 449-452.
1237 65 Hogg, S.J., Motorna, O., Cluse, L.A., Johanson, T.M., Coughlan, H.D., Raviram, R., Myers,
1238 R.M., Costacurta, M., Todorovski, I., Pijpers, L., *et al.* (2021). Targeting histone acetylation dynamics
1239 and oncogenic transcription by catalytic P300/CBP inhibition. Mol Cell *81*, 2183-2200 e2113.
1240 66 Horwitz, G.A., Zhang, K., McBrian, M.A., Grunstein, M., Kurdistani, S.K., and Berk, A.J.
1241 (2008). Adenovirus small e1a alters global patterns of histone modification. Science *321*, 1084-1085.
1242 67 Hottiger, M.O., Felzien, L.K., and Nabel, G.J. (1998). Modulation of cytokine-induced HIV
1243 gene expression by competitive binding of transcription factors to the coactivator p300. EMBO J *17*,
1244 3124-3134.
1245 68 Hsu, E., Pennella, M.A., Zemke, N.R., Eng, C., and Berk, A.J. (2018). Adenovirus E1A
1246 Activation Domain Regulates H3 Acetylation Affecting Varied Steps in Transcription at Different
1247 Viral Promoters. J Virol *92*.
1248 69 Jeppesen, P., and Turner, B.M. (1993). The inactive X chromosome in female mammals is
1249 distinguished by a lack of histone H4 acetylation, a cytogenetic marker for gene expression. Cell *74*,
1250 281-289.
1251 70 Kamei, Y., Xu, L., Heinzel, T., Torchia, J., Kurokawa, R., Gloss, B., Lin, S.C., Heyman,
1252 R.A., Rose, D.W., Glass, C.K., *et al.* (1996). A CBP integrator complex mediates transcriptional
1253 activation and AP-1 inhibition by nuclear receptors. Cell *85*, 403-414.
1254 71 Karanam, B., Jiang, L., Wang, L., Kelleher, N.L., and Cole, P.A. (2006). Kinetic and mass
1255 spectrometric analysis of p300 histone acetyltransferase domain autoacetylation. J Biol Chem *281*,
1256 40292-40301.
1257 72 Kidder, B.L., and Palmer, S. (2012). HDAC1 regulates pluripotency and lineage specific
1258 transcriptional networks in embryonic and trophoblast stem cells. Nucleic Acids Res *40*, 2925-2939.
1259 73 Kraus, W.L., Manning, E.T., and Kadonaga, J.T. (1999). Biochemical analysis of distinct
1260 activation functions in p300 that enhance transcription initiation with chromatin templates. Molecular
1261 and Cellular Biology *19*, 8123-8135.
1262 74 Kribelbauer, J.F., Rastogi, C., Bussemaker, H.J., and Mann, R.S. (2019). Low-Affinity
1263 Binding Sites and the Transcription Factor Specificity Paradox in Eukaryotes. Annu Rev Cell Dev
1264 Biol *35*, 357-379.
1265 75 Krois, A.S., Ferreon, J.C., Martinez-Yamout, M.A., Dyson, H.J., and Wright, P.E. (2016).
1266 Recognition of the disordered p53 transactivation domain by the transcriptional adapter zinc finger
1267 domains of CREB-binding protein. Proc Natl Acad Sci U S A *113*, E1853-1862.
1268 76 Kumar, M., Molkentine, D., Molkentine, J., Bridges, K., Xie, T., Yang, L., Hefner, A., Gao,
1269 M., Bahri, R., Dhawan, A., *et al.* (2021). Inhibition of histone acetyltransferase function
1270 radiosensitizes CREBBP/EP300 mutants via repression of homologous recombination, potentially
1271 targeting a gain of function. Nat Commun *12*, 6340.
1272 77 Ladurner, A.G., Inouye, C., Jain, R., and Tjian, R. (2003). Bromodomains mediate an acetyl-
1273 histone encoded antisilencing function at heterochromatin boundaries. Molecular Cell *11*, 365-376.
1274 78 Larson, A.G., Elnatan, D., Keenen, M.M., Trnka, M.J., Johnston, J.B., Burlingame, A.L.,
1275 Agard, D.A., Redding, S., and Narlikar, G.J. (2017). Liquid droplet formation by HP1alpha suggests a
1276 role for phase separation in heterochromatin. Nature *547*, 236-240.

1277 79 Lee, C.W., Martinez-Yamout, M.A., Dyson, H.J., and Wright, P.E. (2010). Structure of the
1278 p53 transactivation domain in complex with the nuclear receptor coactivator binding domain of
1279 CREB binding protein. Biochemistry *49*, 9964-9971.
1280 80 Li, J., Dong, A., Saydaminova, K., Chang, H., Wang, G., Ochiai, H., Yamamoto, T., and
1281 Pertsinidis, A. (2019). Single-Molecule Nanoscopy Elucidates RNA Polymerase II Transcription at
1282 Single Genes in Live Cells. Cell *178*, 491-506 e428.
1283 81 Li, J., Hsu, A., Hua, Y., Wang, G., Cheng, L., Ochiai, H., Yamamoto, T., and Pertsinidis, A.
1284 (2020). Single-gene imaging links genome topology, promoter-enhancer communication and
1285 transcription control. Nat Struct Mol Biol *27*, 1032-1040.
1286 82 Li, X.Y., MacArthur, S., Bourgon, R., Nix, D., Pollard, D.A., Iyer, V.N., Hechmer, A.,
1287 Simirenko, L., Stapleton, M., Luengo Hendriks, C.L.*, et al.* (2008). Transcription factors bind
1288 thousands of active and inactive regions in the Drosophila blastoderm. PLoS Biol *6*, e27.
1289 83 Lickwar, C.R., Mueller, F., Hanlon, S.E., McNally, J.G., and Lieb, J.D. (2012). Genome-wide
1290 protein-DNA binding dynamics suggest a molecular clutch for transcription factor function. Nature
1291 *484*, 251-255.
1292 84 Lieberman-Aiden, E., van Berkum, N.L., Williams, L., Imakaev, M., Ragoczy, T., Telling,
1293 A., Amit, I., Lajoie, B.R., Sabo, P.J., Dorschner, M.O.*, et al.* (2009). Comprehensive mapping of
1294 long-range interactions reveals folding principles of the human genome. Science *326*, 289-293.
1295 85 Loffreda, A., Jacchetti, E., Antunes, S., Rainone, P., Daniele, T., Morisaki, T., Bianchi, M.E.,
1296 Tacchetti, C., and Mazza, D. (2017). Live-cell p53 single-molecule binding is modulated by C-
1297 terminal acetylation and correlates with transcriptional activity. Nat Commun *8*, 313.
1298 86 Luger, K., Rechsteiner, T.J., and Richmond, T.J. (1999). Preparation of nucleosome core
1299 particle from recombinant histones. Methods Enzymol *304*, 3-19.
1300 87 Luo, J., Li, M., Tang, Y., Laszkowska, M., Roeder, R.G., and Gu, W. (2004). Acetylation of
1301 p53 augments its site-specific DNA binding both in vitro and in vivo. Proc Natl Acad Sci U S A *101*,
1302 2259-2264.
1303 88 Ma, L., Gao, Z., Wu, J., Zhong, B., Xie, Y., Huang, W., and Lin, Y. (2021). Co-condensation
1304 between transcription factor and coactivator p300 modulates transcriptional bursting kinetics. Mol
1305 Cell.
1306 89 Maciejewski, M.W., Schuyler, A.D., Gryk, M.R., Moraru, II, Romero, P.R., Ulrich, E.L.,
1307 Eghbalnia, H.R., Livny, M., Delaglio, F., and Hoch, J.C. (2017). NMRbox: A Resource for
1308 Biomolecular NMR Computation. Biophys J *112*, 1529-1534.
1309 90 Malik, S., and Roeder, R.G. (2010). The metazoan Mediator co-activator complex as an
1310 integrative hub for transcriptional regulation. Nat Rev Genet *11*, 761-772.
1311 91 Marceau, A.H., Brison, C.M., Nerli, S., Arsenault, H.E., McShan, A.C., Chen, E., Lee, H.W.,
1312 Benanti, J.A., Sgourakis, N.G., and Rubin, S.M. (2019). An order-to-disorder structural switch
1313 activates the FoxM1 transcription factor. Elife *8*.
1314 92 Merika, M., Williams, A.J., Chen, G., Collins, T., and Thanos, D. (1998). Recruitment of
1315 CBP/p300 by the IFN beta enhanceosome is required for synergistic activation of transcription. Mol
1316 Cell *1*, 277-287.
1317 93 Meyer, M.E., Gronemeyer, H., Turcotte, B., Bocquel, M.T., Tasset, D., and Chambon, P.
1318 (1989). Steroid hormone receptors compete for factors that mediate their enhancer function. Cell *57*,
1319 433-442.
1320 94 Migl, D., Kschonsak, M., Arthur, C.P., Khin, Y., Harrison, S.C., Ciferri, C., and Dimitrova,
1321 Y.N. (2020). Cryoelectron Microscopy Structure of a Yeast Centromeric Nucleosome at 2.7 A
1322 Resolution. Structure *28*, 363-370 e363.
1323 95 Miller Jenkins, L.M., Feng, H., Durell, S.R., Tagad, H.D., Mazur, S.J., Tropea, J.E., Bai, Y.,
1324 and Appella, E. (2015). Characterization of the p300 Taz2-p53 TAD2 complex and comparison with
1325 the p300 Taz2-p53 TAD1 complex. Biochemistry *54*, 2001-2010.
1326 96 Miller, T.C., Simon, B., Rybin, V., Grotsch, H., Curtet, S., Khochbin, S., Carlomagno, T., and
1327 Muller, C.W. (2016). A bromodomain-DNA interaction facilitates acetylation-dependent bivalent
1328 nucleosome recognition by the BET protein BRDT. Nat Commun *7*, 13855.
1329 97 Mirny, L., Slutsky, M., Wunderlich, Z., Tafvizi, A., Leith, J., and Kosmrlj, A. (2009). How a
1330 protein searches for its site on DNA: the mechanism of facilitated diffusion. Journal of Physics A:
1331 Mathematical and Theoretical *42*, 434013.

1332 98 Misteli, T. (2020). The Self-Organizing Genome: Principles of Genome Architecture and
1333 Function. Cell *183*, 28-45.
1334 99 Monahan, K., Horta, A., and Lomvardas, S. (2019). LHX2- and LDB1-mediated trans
1335 interactions regulate olfactory receptor choice. Nature *565*, 448-453.
1336 100 Mueller, W.G., Walker, D., Hager, G.L., and McNally, J.G. (2001). Large-scale chromatin
1337 decondensation and recondensation regulated by transcription from a natural promoter. Mol Biol Cell
1338 *12*, 357a-357a.
1339 101 Mukherjee, S.P., Behar, M., Birnbaum, H.A., Hoffmann, A., Wright, P.E., and Ghosh, G.
1340 (2013). Analysis of the RelA:CBP/p300 interaction reveals its involvement in NF-kappaB-driven
1341 transcription. PLoS Biol *11*, e1001647.
1342 102 Narita, T., Ito, S., Higashijima, Y., Chu, W.K., Neumann, K., Walter, J., Satpathy, S.,
1343 Liebner, T., Hamilton, W.B., Maskey, E.*, et al.* (2021). Enhancers are activated by p300/CBP
1344 activity-dependent PIC assembly, RNAPII recruitment, and pause release. Mol Cell *81*, 2166-2182
1345 e2166.
1346 103 Nora, E.P., Lajoie, B.R., Schulz, E.G., Giorgetti, L., Okamoto, I., Servant, N., Piolot, T., van
1347 Berkum, N.L., Meisig, J., Sedat, J.*, et al.* (2012). Spatial partitioning of the regulatory landscape of
1348 the X-inactivation centre. Nature *485*, 381-385.
1349 104 Nuebler, J., Fudenberg, G., Imakaev, M., Abdennur, N., and Mirny, L.A. (2018). Chromatin
1350 organization by an interplay of loop extrusion and compartmental segregation. Proc Natl Acad Sci U
1351 S A *115*, E6697-E6706.
1352 105 Ortega, E., Rengachari, S., Ibrahim, Z., Hoghoughi, N., Gaucher, J., Holehouse, A.S.,
1353 Khochbin, S., and Panne, D. (2018). Transcription factor dimerization activates the p300
1354 acetyltransferase. Nature *562*, 538-544.
1355 106 Ozenne, V., Bauer, F., Salmon, L., Huang, J.R., Jensen, M.R., Segard, S., Bernado, P.,
1356 Charavay, C., and Blackledge, M. (2012). Flexible-meccano: a tool for the generation of explicit
1357 ensemble descriptions of intrinsically disordered proteins and their associated experimental
1358 observables. Bioinformatics *28*, 1463-1470.
1359 107 Panne, D. (2008). The enhanceosome. Curr Opin Struct Biol *18*, 236-242.
1360 108 Panne, D., Maniatis, T., and Harrison, S.C. (2007). An atomic model of the interferon-beta
1361 enhanceosome. Cell *129*, 1111-1123.
1362 109 Pelka, P., Ablack, J.N., Torchia, J., Turnell, A.S., Grand, R.J., and Mymryk, J.S. (2009).
1363 Transcriptional control by adenovirus E1A conserved region 3 via p300/CBP. Nucleic Acids Res *37*,
1364 1095-1106.
1365 110 Petoukhov, M.V., Franke, D., Shkumatov, A.V., Tria, G., Kikhney, A.G., Gajda, M., Gorba,
1366 C., Mertens, H.D., Konarev, P.V., and Svergun, D.I. (2012). New developments in the program
1367 package for small-angle scattering data analysis. J Appl Crystallogr *45*, 342-350.
1368 111 Pivot-Pajot, C., Caron, C., Govin, J., Vion, A., Rousseaux, S., and Khochbin, S. (2003).
1369 Acetylation-dependent chromatin reorganization by BRDT, a testis-specific bromodomain-containing
1370 protein. Mol Cell Biol *23*, 5354-5365.
1371 112 Plevin, M.J., Mills, M.M., and Ikura, M. (2005). The LxxLL motif: a multifunctional binding
1372 sequence in transcriptional regulation. Trends Biochem Sci *30*, 66-69.
1373 113 Portuguez, A.S., Grbesa, I., Tal, M., Deitch, R., Raz, D., Weismann, R., Schwartz, M., Loza,
1374 O., Sung, M.-H., Kaplan, T.*, et al.* (2019). Gene activation and repression by the glucocorticoid
1375 receptor are mediated by sequestering Ep300 and two modes of chromatin binding. bioRxiv.
1376 114 Rada-Iglesias, A., Bajpai, R., Swigut, T., Brugmann, S.A., Flynn, R.A., and Wysocka, J.
1377 (2010). A unique chromatin signature uncovers early developmental enhancers in humans. Nature.
1378 115 Reiter, F., Wienerroither, S., and Stark, A. (2017). Combinatorial function of transcription
1379 factors and cofactors. Curr Opin Genet Dev *43*, 73-81.
1380 116 Reynoird, N., Schwartz, B.E., Delvecchio, M., Sadoul, K., Meyers, D., Mukherjee, C., Caron,
1381 C., Kimura, H., Rousseaux, S., Cole, P.A.*, et al.* (2010). Oncogenesis by sequestration of CBP/p300
1382 in transcriptionally inactive hyperacetylated chromatin domains. EMBO J *29*, 2943-2952.
1383 117 Rosencrance, C.D., Ammouri, H.N., Yu, Q., Ge, T., Rendleman, E.J., Marshall, S.A., and
1384 Eagen, K.P. (2020). Chromatin Hyperacetylation Impacts Chromosome Folding by Forming a
1385 Nuclear Subcompartment. Mol Cell *78*, 112-126 e112.

118 Rowley, M.J., and Corces, V.G. (2018). Organizational principles of 3D genome architecture. Nat Rev Genet *19*, 789-800.
119 Rundlett, S.E., Carmen, A.A., Kobayashi, R., Bavykin, S., Turner, B.M., and Grunstein, M. (1996). HDA1 and RPD3 are members of distinct yeast histone deacetylase complexes that regulate silencing and transcription. Proc Natl Acad Sci U S A *93*, 14503-14508.
120 Sabari, B.R., Dall'Agnese, A., Boija, A., Klein, I.A., Coffey, E.L., Shrinivas, K., Abraham, B.J., Hannett, N.M., Zamudio, A.V., Manteiga, J.C., *et al.* (2018). Coactivator condensation at super-enhancers links phase separation and gene control. Science *361*.
121 Schumann, F.H., Riepl, H., Maurer, T., Gronwald, W., Neidig, K.P., and Kalbitzer, H.R. (2007). Combined chemical shift changes and amino acid specific chemical shift mapping of protein-protein interactions. J Biomol NMR *39*, 275-289.
122 Schwartz, B.E., Hofer, M.D., Lemieux, M.E., Bauer, D.E., Cameron, M.J., West, N.H., Agoston, E.S., Reynoird, N., Khochbin, S., Ince, T.A., *et al.* (2011). Differentiation of NUT midline carcinoma by epigenomic reprogramming. Cancer Research *71*, 2686-2696.
123 Schwarzer, W., Abdennur, N., Goloborodko, A., Pekowska, A., Fudenberg, G., Loe-Mie, Y., Fonseca, N.A., Huber, W., C, H.H., Mirny, L., *et al.* (2017). Two independent modes of chromatin organization revealed by cohesin removal. Nature *551*, 51-56.
124 Sheahan, T.W., Major, V., Webb, K.M., Bryan, E., and Voigt, P. (2020). The TAZ2 domain of CBP/p300 directs acetylation towards H3K27 within chromatin. bioRxiv.
125 Shen, Y., and Bax, A. (2013). Protein backbone and sidechain torsion angles predicted from NMR chemical shifts using artificial neural networks. J Biomol NMR *56*, 227-241.
126 Shin, Y., Chang, Y.C., Lee, D.S.W., Berry, J., Sanders, D.W., Ronceray, P., Wingreen, N.S., Haataja, M., and Brangwynne, C.P. (2018). Liquid Nuclear Condensates Mechanically Sense and Restructure the Genome. Cell *175*, 1481-1491 e1413.
127 Shiota, H., Barral, S., Buchou, T., Tan, M., Coute, Y., Charbonnier, G., Reynoird, N., Boussouar, F., Gerard, M., Zhu, M., *et al.* (2018). Nut Directs p300-Dependent, Genome-Wide H4 Hyperacetylation in Male Germ Cells. Cell Rep *24*, 3477-3487 e3476.
128 Shogren-Knaak, M., Ishii, H., Sun, J.M., Pazin, M.J., Davie, J.R., and Peterson, C.L. (2006). Histone H4-K16 acetylation controls chromatin structure and protein interactions. Science *311*, 844-847.
129 Shrinivas, K., Sabari, B.R., Coffey, E.L., Klein, I.A., Boija, A., Zamudio, A.V., Schuijers, J., Hannett, N.M., Sharp, P.A., Young, R.A., *et al.* (2019). Enhancer Features that Drive Formation of Transcriptional Condensates. Mol Cell *75*, 549-561 e547.
130 Slaughter, M.J., Shanle, E.K., Khan, A., Chua, K.F., Hong, T., Boxer, L.D., Allis, C.D., Josefowicz, S.Z., Garcia, B.A., Rothbart, S.B., *et al.* (2021). HDAC inhibition results in widespread alteration of the histone acetylation landscape and BRD4 targeting to gene bodies. Cell Rep *34*, 108638.
131 Solovei, I., Thanisch, K., and Feodorova, Y. (2016). How to rule the nucleus: divide et impera. Curr Opin Cell Biol *40*, 47-59.
132 Spilianakis, C.G., Lalioti, M.D., Town, T., Lee, G.R., and Flavell, R.A. (2005). Interchromosomal associations between alternatively expressed loci. Nature *435*, 637-645.
133 Staller, M.V., Holehouse, A.S., Swain-Lenz, D., Das, R.K., Pappu, R.V., and Cohen, B.A. (2018). A High-Throughput Mutational Scan of an Intrinsically Disordered Acidic Transcriptional Activation Domain. Cell Syst *6*, 444-455 e446.
134 Strahl, B.D., and Allis, C.D. (2000). The language of covalent histone modifications. Nature *403*, 41-45.
135 Strickfaden, H., Tolsma, T.O., Sharma, A., Underhill, D.A., Hansen, J.C., and Hendzel, M.J. (2020). Condensed Chromatin Behaves like a Solid on the Mesoscale In Vitro and in Living Cells. Cell *183*, 1772-1784 e1713.
136 Strom, A.R., Biggs, R.J., Banigan, E.J., Wang, X., Chiu, K., Herman, C., Collado, J., Yue, F., Ritland Politz, J.C., Tait, L.J., *et al.* (2021). HP1alpha is a chromatin crosslinker that controls nuclear and mitotic chromosome mechanics. Elife *10*.
137 Strom, A.R., Emelyanov, A.V., Mir, M., Fyodorov, D.V., Darzacq, X., and Karpen, G.H. (2017). Phase separation drives heterochromatin domain formation. Nature *547*, 241-245.

138 Taddei, A., Maison, C., Roche, D., and Almouzni, G. (2001). Reversible disruption of pericentric heterochromatin and centromere function by inhibiting deacetylases. Nat Cell Biol *3*, 114-120.
139 Therizols, P., Illingworth, R.S., Courilleau, C., Boyle, S., Wood, A.J., and Bickmore, W.A. (2014). Chromatin decondensation is sufficient to alter nuclear organization in embryonic stem cells. Science *346*, 1238-1242.
140 Thompson, P.R., Wang, D., Wang, L., Fulco, M., Pediconi, N., Zhang, D., An, W., Ge, Q., Roeder, R.G., Wong, J.*, et al.* (2004). Regulation of the p300 HAT domain via a novel activation loop. Nat Struct Mol Biol *11*, 308-315.
141 Toth, K.F., Knoch, T.A., Wachsmuth, M., Frank-Stohr, M., Stohr, M., Bacher, C.P., Muller, G., and Rippe, K. (2004). Trichostatin A-induced histone acetylation causes decondensation of interphase chromatin. J Cell Sci *117*, 4277-4287.
142 Triezenberg, S.J., Kingsbury, R.C., and McKnight, S.L. (1988). Functional dissection of VP16, the trans-activator of herpes simplex virus immediate early gene expression. Genes Dev *2*, 718-729.
143 Tumbar, T., Belmont, A.S., and Sudlow, G.P. (1999a). Targeting the VP16 acidic activation domain induces chances in large-scale chromatin structure and nuclear positioning. Mol Biol Cell *10*, 281a-281a.
144 Tumbar, T., Sudlow, G., and Belmont, A.S. (1999b). Large-scale chromatin unfolding and remodeling induced by VP16 acidic activation domain. J Cell Biol *145*, 1341-1354.
145 van de Werken, H.J.G., Haan, J.C., Feodorova, Y., Bijos, D., Weuts, A., Theunis, K., Holwerda, S.J.B., Meuleman, W., Pagie, L., Thanisch, K.*, et al.* (2017). Small chromosomal regions position themselves autonomously according to their chromatin class. Genome Res *27*, 922-933.
146 Vogelauer, M., Wu, J., Suka, N., and Grunstein, M. (2000). Global histone acetylation and deacetylation in yeast. Nature *408*, 495-498.
147 Wang, F., Marshall, C.B., Yamamoto, K., Li, G.Y., Gasmi-Seabrook, G.M., Okada, H., Mak, T.W., and Ikura, M. (2012a). Structures of KIX domain of CBP in complex with two FOXO3a transactivation domains reveal promiscuity and plasticity in coactivator recruitment. Proc Natl Acad Sci U S A *109*, 6078-6083.
148 Wang, L., Gao, Y., Zheng, X., Liu, C., Dong, S., Li, R., Zhang, G., Wei, Y., Qu, H., Li, Y.*, et al.* (2019). Histone Modifications Regulate Chromatin Compartmentalization by Contributing to a Phase Separation Mechanism. Mol Cell *76*, 646-659 e646.
149 Wang, R., Li, Q., Helfer, C.M., Jiao, J., and You, J. (2012b). Bromodomain protein Brd4 associated with acetylated chromatin is important for maintenance of higher-order chromatin structure. J Biol Chem *287*, 10738-10752.
150 Wang, R., and You, J. (2015). Mechanistic analysis of the role of bromodomain-containing protein 4 (BRD4) in BRD4-NUT oncoprotein-induced transcriptional activation. J Biol Chem *290*, 2744-2758.
151 Wang, Z., Zang, C., Cui, K., Schones, D.E., Barski, A., Peng, W., and Zhao, K. (2009). Genome-wide mapping of HATs and HDACs reveals distinct functions in active and inactive genes. Cell *138*, 1019-1031.
152 Weinert, B.T., Narita, T., Satpathy, S., Srinivasan, B., Hansen, B.K., Scholz, C., Hamilton, W.B., Zucconi, B.E., Wang, W.W., Liu, W.R.*, et al.* (2018). Time-Resolved Analysis Reveals Rapid Dynamics and Broad Scope of the CBP/p300 Acetylome. Cell *174*, 231-244 e212.
153 Whyte, W.A., Bilodeau, S., Orlando, D.A., Hoke, H.A., Frampton, G.M., Foster, C.T., Cowley, S.M., and Young, R.A. (2012). Enhancer decommissioning by LSD1 during embryonic stem cell differentiation. Nature *482*, 221-225.
154 Wojciak, J.M., Martinez-Yamout, M.A., Dyson, H.J., and Wright, P.E. (2009). Structural basis for recruitment of CBP/p300 coactivators by STAT1 and STAT2 transactivation domains. EMBO J *28*, 948-958.
155 Wu, S.Y., Lee, A.Y., Lai, H.T., Zhang, H., and Chiang, C.M. (2013). Phospho switch triggers Brd4 chromatin binding and activator recruitment for gene-specific targeting. Mol Cell *49*, 843-857.
156 Yan, J., Diaz, J., Jiao, J., Wang, R., and You, J. (2011). Perturbation of BRD4 protein function by BRD4-NUT protein abrogates cellular differentiation in NUT midline carcinoma. J Biol Chem *286*, 27663-27675.

157 Zamudio, A.V., Dall'Agnese, A., Henninger, J.E., Manteiga, J.C., Afeyan, L.K., Hannett, N.M., Coffey, E.L., Li, C.H., Oksuz, O., Sabari, B.R., *et al.* (2019). Mediator Condensates Localize Signaling Factors to Key Cell Identity Genes. Mol Cell *76*, 753-766 e756.
158 Zhang, K. (2016). Gctf: Real-time CTF determination and correction. Journal of Structural Biology *193*, 1-12.
159 Zhang, T., Zhang, Z., Dong, Q., Xiong, J., and Zhu, B. (2020). Histone H3K27 acetylation is dispensable for enhancer activity in mouse embryonic stem cells. Genome Biol *21*, 45.
160 Zhang, Y., Brown, K., Yu, Y., Ibrahim, Z., Zandian, M., Xuan, H., Ingersoll, S., Lee, T., Ebmeier, C.C., Liu, J., *et al.* (2021). Nuclear condensates of p300 formed though the structured catalytic core can act as a storage pool of p300 with reduced HAT activity. Nat Commun *12*, 4618.
161 Zhang, Y., Xue, Y., Shi, J., Ahn, J., Mi, W., Ali, M., Wang, X., Klein, B.J., Wen, H., Li, W., *et al.* (2018). The ZZ domain of p300 mediates specificity of the adjacent HAT domain for histone H3. Nat Struct Mol Biol *25*, 841-849.
162 Zhao, R., Nakamura, T., Fu, Y., Lazar, Z., and Spector, D.L. (2011). Gene bookmarking accelerates the kinetics of post-mitotic transcriptional re-activation. Nature Cell Biology *13*, 1295-U1239.
163 Zheng, S.Q., Palovcak, E., Armache, J.P., Verba, K.A., Cheng, Y., and Agard, D.A. (2017). MotionCor2: anisotropic correction of beam-induced motion for improved cryo-electron microscopy. Nat Methods *14*, 331-332.
164 Zivanov, J., Nakane, T., Forsberg, B.O., Kimanius, D., Hagen, W.J., Lindahl, E., and Scheres, S.H. (2018). New tools for automated high-resolution cryo-EM structure determination in RELION-3. Elife *7*.
165 Zylicz, J.J., Bousard, A., Zumer, K., Dossin, F., Mohammad, E., da Rocha, S.T., Schwalb, B., Syx, L., Dingli, F., Loew, D., *et al.* (2019). The Implication of Early Chromatin Changes in X Chromosome Inactivation. Cell *176*, 182-197 e123.

Acknowledgements We thank Christos Savva and TJ Ragan for CryoEM support. We thank Nathan Cowieson from the B21 BioSAXS beamline of the Diamond Light Source; Yingming Zhao and Jinjun Gao for mass spectroscopy analysis; Luke Bailey, Sarah Northall and Dipti Vashi for help with histone preparations. Michael K. Rosen for plasmids encoding GFP-$(Bomo)_5$ and GFP-$(Bromo)_5$ N140A; Stephen M. Hinshaw and Stephen C. Harrison for plasmids encoding *S. cerevisiae* histones; Andrew Flaus for *H. sapiens* histones; Timothy J. Richmond for histone H4 mutant plasmids; Andy Turnell for E1A plasmids. Work in the S.K. laboratory was supported by ANR Episperm4 program, by Plan Cancer Pitcher, by MSD Avenir ERICAN programs, by the Cancer ITMO (Multi-Organisation Thematic Institute) of the French Alliance for Life Sciences and Health (AVIESAN) MIC program, by the "Université Grenoble Alpes" ANR-15-IDEX-02 SYMER and LIFE programs and by Fondation ARC program RF20190208471. Work in the T.S. laboratory was supported by the BBSRC (BB/S019510/1; BB/R016275/1). Work in the D.P. laboratory was supported by grants from the Worldwide Cancer Research [16-0280], the Wellcome Trust [221881/Z/20/Z], Instruct-ERIC [PID: 18571] and the Medical Research Council [MR/W001667/1].

Author contributions Z.I. designed and performed most experiments, analysed and validated the data with support by L.F. T.W., O.D. N.H and N.R performed cell biology experiments. N.S. performed NMR experiments. A.R performed chromatin analyses *in vitro*. Y. Z. and J. G. performed mass spectroscopy analysis. T.S., M.B., and S.K. provided supervision, funding acquisition and commented on the draft. D.P. was involved in conceptualization, supervision, project administration, funding acquisition. Z.I and D.P. wrote the original and revised drafts with input from all authors.

Competing interests: Y. Z. is a founder, board member, advisor to, and inventor on patents licensed to PTM Biolabs Inc (Hangzhou, China and Chicago, IL) and Maponos Therapeutics Inc. (Chicago, IL). The other authors declare no competing interests.